(4)

AFGL-TR-87-0269 AD-A188 919

AN ASSESSMENT OF THE APPLICATION OF *IN SITU* ION-DENSITY DATA FROM DMSP TO MODELING OF TRANSIONOSPHERIC SCINTILLATION

James A. Secan
NorthWest Research Associates, Inc.
P.O. Box 3027
Bellevue, Washington 98009

15 September 1987

Scientific Report No. 1

Approved for public release; distribution unlimited

Prepared for:

AIR FORCE GEOPHYSICS LABORATORY
AIR FORCE SYSTEMS COMMAND
UNITED STATES AIR FORCE
HANSCOM AFB, MASSACHUSETTS 0173

"This technical report has been reviewed and is approved for publication."

Christopher Sherman
CHRISTOPHER SHERMAN
Contract Manager

William K. Vickery
WILLIAM K. VICKERY
Acting Branch Chief

FOR THE COMMANDER

John E. Rasmussen
JOHN E. RASMUSSEN
Acting Division Director

This document has been reviewed by the ESD Public Affairs Office (PA) and is releasable to the National Technical Information Service (NTIS).

Qualified requestors may obtain additional copies from the Defense Technical Information Center. All others should apply to the National Technical Information Service.

If your address has changed, or if you wish to be removed from the mailing list, or if the addressee is no longer employed by your organization, please notify AFGL/DAA, Hanscom AFB, MA 01731. This will assist us in maintaining a current mailing list.

Do not return copies of this report unless contractual obligations or notices on a specific document requires that it be returned.

REPORT DOCUMENTATION PAGE

1a. REPORT SECURITY CLASSIFICATION Unclassified	1b. RESTRICTIVE MARKINGS
2a. SECURITY CLASSIFICATION AUTHORITY	3. DISTRIBUTION/AVAILABILITY OF REPORT Approved for public release. Distribution unlimited.
2b. DECLASSIFICATION/DOWNGRADING SCHEDULE	
4. PERFORMING ORGANIZATION REPORT NUMBER(S) NWRA-CR-87-R017	5. MONITORING ORGANIZATION REPORT NUMBER(S) AFGL-TR-87-0269
6a. NAME OF PERFORMING ORGANIZATION Northwest Research Associates, Inc. 6b. OFFICE SYMBOL (If applicable) CR Division	7a. NAME OF MONITORING ORGANIZATION Air Force Geophysics Laboratory
6c. ADDRESS (City, State, and ZIP Code) P.O. Box 3027 Bellevue, WA 98009	7b. ADDRESS (City, State, and ZIP Code) Hanscom AFB, MA 01731
8a. NAME OF FUNDING/SPONSORING ORGANIZATION 8b. OFFICE SYMBOL (If applicable)	9. PROCUREMENT INSTRUMENT IDENTIFICATION NUMBER F19628-86-C-0195
8c. ADDRESS (City, State, and ZIP Code)	10. SOURCE OF FUNDING NUMBERS PROGRAM ELEMENT NO. 62101F; PROJECT NO. 4643; TASK NO. 09; WORK UNIT ACCESSION NO. AI

11. TITLE (Include Security Classification)
An Assessment of the Application of In Situ Ion-density data from DMSP to modeling of Transionospheric Scintillation

12. PERSONAL AUTHOR(S)
Secan, James A.

13a. TYPE OF REPORT	13b. TIME COVERED	14. DATE OF REPORT (Year, Month, Day)	15. PAGE COUNT
Scientific No. 1	FROM 86Sep15 TO 87Sep14	15 September 1987	80

16. SUPPLEMENTARY NOTATION

17. COSATI CODES			18. SUBJECT TERMS (Continue on reverse if necessary and identify by block number)
FIELD	GROUP	SUB-GROUP	
04	0		Ionosphere, Ionospheric Scintillation, Radiowave Scint-
20	14		illation, Defense Meteorology Satellite Program (DMSP)

19. ABSTRACT (Continue on reverse if necessary and identify by block number)

Modern military communication, navigation, and surveillance systems depend on reliable, noise-free transionospheric radio frequency channels. They can be severely impacted by small-scale electron density irregularities in the ionosphere which cause both phase and amplitude scintillation. Basic tools used in planning and mitigation schemes are climatological in nature and thus may greatly over- and under-estimate the effects of scintillation in a given scenario. This report describes the first year of an investigation into the feasibility of using *in situ* observations of the ionosphere from the USAF DMSP satellite to calculate estimates of irregularity parameters which could be used to update scintillation models in near real-time. Methods for calculating estimates of the height-integrated irregularity strength parameter (C_kL) from DMSP SSIES data are described, and the results of parametric studies of the effects of errors or uncertainties in both the observed quantities and the methods used to calculate the estimates of C_kL are presented.

20. DISTRIBUTION/AVAILABILITY OF ABSTRACT ☐ UNCLASSIFIED/UNLIMITED ☐ SAME AS RPT. ☐ DTIC USERS	21. ABSTRACT SECURITY CLASSIFICATION Unclassified	
22a. NAME OF RESPONSIBLE INDIVIDUAL Christopher Sherman	22b. TELEPHONE (Include Area Code)	22c. OFFICE SYMBOL AFGL/LIS

DD FORM 1473, 84 MAR — 83 APR edition may be used until exhausted. All other editions are obsolete.

TABLE OF CONTENTS

LIST OF FIGURES

LIST OF TABLES

PREFACE

This report describes the work completed during the first year of a three-year investigation into the feasibility of using *in-situ* observations of the ionosphere from the DMSP SSIES sensors to calculate parameters which characterize ionospheric scintillation effects. This work is part of a larger effort with an overall objective of providing the USAF Air Weather Service with the capability of observing ionospheric scintillations, and the plasma density irregularities which cause the scintillations, in near real-time and updating models of ionospheric scintillation with these observations.

1. INTRODUCTION

Many modern military systems used for communications, command and control, navigation, and surveillance depend on reliable and relatively noise-free transmission of radiowave signals through the earth's ionosphere. Small-scale irregularities in the ionospheric density can cause severe distortion, known as radiowave scintillation, of both the amplitude and phase of these signals. A basic tool used in estimating these effects on systems is a computer program, WBMOD, based on a single-scatter phase-screen propagation model and a number of empirical models of the global morphology of ionospheric density irregularities. An inherent weakness of WBMOD is that the irregularity models provide median estimates for parameters with large dynamic ranges, which can lead to large under- and over-estimation of the effects of the ionospheric irregularities on a system.

One solution to this problem, at least for near real-time estimates, is to update the WBMOD irregularity models with observations of the various parameters modeled. One proposed source for these observations is from the *in situ* plasma density monitor to be flown on the Defense Meteorology Satellite Program (DMSP) satellites. This study is designed to assess the applicability of this data set to real-time updates of the WBMOD models. There are two primary objectives:

(1) Develop and refine techniques for generating estimates of parameters which characterize ionospheric scintillation from *in situ* observations of the ionospheric plasma from the DMSP SSIES sensors.

(2) Determine if the parameters calculated from the SSIES data can be used to determine the scintillation effects on a transionospheric radiowave signal.

This report describes the results obtained during the first year of the study. The focus during this year was on developing the techniques to be used for calculating scintillation parameters from the SSIES data and making determinations of the uncertainties involved in these calculations.

2. BACKGROUND

The propagation model used in the WBMOD program (based on weak-scatter phase-screen theory[1]) characterizes the ionospheric electron density irregularities which cause scintillation via eight independent parameters[2]:

(1) The irregularity axial ratio along the direction of the ambient geomagnetic field, a.

(2) The irregularity axial ratio perpendicular to the direction of the ambient geomagnetic field, b.

(3) The angle between sheet-like irregularity structures and geomagnetic L shells, δ.

(4) The height of the equivalent phase screen above the earth's surface, h_p.

(5) The *in situ* irregularity drift velocity, $\underline{v}_d$.

(6) The outer scale of the irregularity spectrum, α_o.

(7) The slope of a power-law distribution which describes the one-dimensional power density spectrum (PDS) of the irregularities, q.

(8) The height-integrated strength parameter, C_kL.

The first three parameters (a, b, and δ) and the direction of the ambient geomagnetic field specify the propagation geometry, while the last three (α_o, q, and C_kL) specify the spectral characteristics of the irregularities.

It may be possible to obtain estimates for the values of three of these parameters from the DMSP SSIES sensors: $\underline{v}_d$ (from the SSIES ion Drift Meter (DM)), and q and C_kL (from the SSIES ion Scintillation Meter (SM)). In this study, we will focus on the estimation of C_kL from this data set and consider q and $\underline{v}_d$ only in terms of the effects of uncertainties in these parameters on the estimates of C_kL. Of the eight parameters, C_kL varies the most as a function of location and time, and has the most profound effect of the accuracy of estimates of scintillation levels made by the WBMOD model.

In the phase-screen propagation theory used in WBMOD,[2] the C_kL parameter is actually the product of two parameters: C_k, the threedimensional spectral "strength" of the electron density irregularities at a scale size of 1000km (related to the structure constant used in classical turbulence theory); and L, the thickness of the irregularity layer.* The models in WBMOD were obtained from analysis of phase scintillation data from the WIDEBAND and HiLat satellites, which will provide estimates of the height-integrated value of C_kL rather than independent measures of C_k and L. Because of this, the model was developed for C_kL rather than for C_k and L separately.

The calculation of an estimate of the C_kL parameter from topside *in situ* ion density observations requires two operations. First, an estimate of C_k at the satellite altitude is made from a finite-length time series of density measurements. Second, the estimate of C_k is converted to an estimate of C_kL in some fashion which will account for both the thickness of the irregularity layer and the variation of C_k, or $\langle \Delta N_e^2 \rangle$, within the layer.

The data set from which the estimates of these parameters are to be obtained will be collected by three instruments in the DMSP SSIES (Special Sensor for Ions, Electrons, and Scintillation) sensor package. This data set will contain the following *in situ* observations:

(1) High time-resolution (24 samples/sec) measurements of the ion density and measurements of the ion density irregularity PDS at high fluctuating frequencies from the ion Scintillation Meter (SM).[3]

(2) Measurements of the horizontal and vertical cross-track ion drift velocities from the ion Drift Meter (DM).[3]

(3) Measurements of the ion and electron temperatures, the densities of O+ and the dominant light ion (H+ or He+), and the horizontal ram ion drift velocity from the ion Retarding Potential Analyzer (RPA).[4]

---

* The cited reference develops the theory in terms of an earlier definition of the strength parameter, C_s, which is defined at a scale size of 2π meters. It is related to C_k via $C_s = (2\pi/1000)^{q+2}\,C_k$.

The basic data of this set is the high time-resolution density data from the SM which will be used to generate estimates of the irregularity PDS. The drift velocity measurements from the DM and RPA will be used in calculating an estimate of C_k from parameters obtained from the PDS, and the other measurements from the RPA will be used in calculating C_kL from C_k.

The project is divided into two phases. In the first phase, techniques for calculating estimates of C_kL from the SSIES data set will be developed, and parametric studies will be conducted to determine the uncertainties in the final C_kL estimates due to uncertainties in the parameters and procedures used to calculate the estimates. There will be no DMSP SSIES data available during this phase, as the first is due to be launched in mid-1987, so these studies will be made using other data sources.

The second phase, which will begin after the scheduled DMSP launch, will focus on how well these techniques work. There will be two investigations conducted during this phase: (1) an analysis of C_kL values calculated for selected DMSP orbits, and (2) an assessment of the validity of the basic assumptions made in order to calculate an estimate of C_kL from a C_k measurement made at an altitude of 830km. The cornerstone of the second investigation is planned to be at least one coincident measurement campaign during which ionospheric profile data from an incoherent radar, phase scintillation data from a satellite beacon, and *in situ* ion-density irregularity observations near the F2 peak would be collected in near-coincidence (time and location) with a DMSP orbit.

3. PARAMETRIC STUDIES: UNCERTAINTIES IN C_k

The objective of the first set of parametric studies was to determine the level of uncertainty in estimates of C_k from several sources. Three studies were conducted: (1) an investigation of uncertainties in C_k calculated from T_1 and q due to uncertainties in T_1 and q, (2) an investigation of uncertainties in C_k calculated from $\langle \Delta N_e^2 \rangle$ due to uncertainties in the cutoff frequency, f_c, and q, and (3) an investigation of uncertainties in C_k due to uncertainties in the effective satellite velocity, v_p.

3.1 Calculation of C_k

According to phase-screen theory,[2] an estimate for C_k can be calculated from an *in situ* measurement of the ionospheric electron density from

$$C_k = 5.0\times10^8 \, q \left(\frac{10^3}{v_p} \right)^{q-1} T_1 \qquad [1]$$

where q and T_1 are the slope and intercept of a log-linear fit to the Power Density Spectrum (PDS) of the data sample, and v_p is the effective velocity of the satellite with respect to the irregularities. This last parameter is defined in a coordinate system defined by the irregularities and is given by

$$v_p = \underline{v}^T \underline{\underline{C}} \, \underline{v} \qquad [2]$$

where $\underline{v}$ is the vector velocity of the satellite and $\underline{\underline{C}}$ is a transformation matrix derived from a generalized irregularity model.[5] Equation [1] can also be written in terms of the variance of the electron density irregularities, $\langle \Delta N_e^2 \rangle$, as

$$C_k = 2.5\times10^8 \, q(q-1) \left(\frac{10^3 f_c}{v_p} \right)^{q-1} \langle \Delta N_e^2 \rangle \qquad [3]$$

where f_c is a low-frequency cutoff set by whatever detrending process was used in calculating $\langle \Delta N_e^2 \rangle$, which establishes the largest scale sizes included in the variance. In this context, "detrending" includes all processing done to the data prior to calculation of the variance, including selection of a finite-length data set.

3.2 Uncertainties in C_k Calculated from T_1 and q

The effects of various processing techniques which are used in calculating the PDS were investigated using both simulated data sets with known spectral characteristics and actual observations of ionospheric irregularities. The purpose of this study was to determine the optimum analysis methodology for obtaining estimates of the power-law parameters q and T_1 for use in calculating C_k. This study is similar to a recent study of the relative merits of deriving estimates of the PDS from FFTs and from the Maximum Entropy Method (MEM),[6] but this study will focus solely on the FFT method and will include the effects of the various processing methods on the strength parameter, T_1, as well as on the slope parameter, q.

There is currently no set of data from a DMSP SSIES sensor as the first of these is scheduled to be on DMSP satellite F8, due for launch in mid-1987. Two types of data sets were used in these parametric studies: (1) simulated density-data sets constructed with known power density spectra, and (2) a sample of phase scintillation data taken from the DNA WIDEBAND satellite experiment. Details on the construction of the simulated data sets and on the WIDEBAND phase scintillation data are given in Appendix A to this report.

All realizations for each of the data sets, simulated and real, were processed in the following manner:

1. The ΔN data from the simulation data sets were converted to simulated plasma density samples using a T_1 of 10^{16} and a mean density value of 10^5 el/cm^3. Optionally, the low-frequency trend terms are added on.

2. The plasma density sample (512 points) is then detrended using one of three detrenders (linear trend removal (LDET), quadratic trend removal (QDET), or end-matching a removal of the residual mean (EMMR)).

3. The detrended data are then windowed using one of eleven windows (a rectangular window (essentially no window) or one of ten split-bell cosine windows ranging from a 10% taper to a 100% taper).

4. An estimate of the PDS of the sample is obtained from an FFT of the windowed, detrended data.

5. The PDS is optionally smoothed using one of four moving, centered smoothing functions using binomial weights (3-, 5-, 7-, or 9-point smoothing).

6. Estimates of T_1 and q are obtained from a log-linear fit to the PDS over the frequency range 0.2 to 7.0 Hz.

The results of this processing for each realization (T_1, q, and $\langle \Delta N_e{}^2 \rangle^{1/2}$ at various steps in the processing) are stored in an analysis data base for further reduction. A total of 132 analyses (3 detrenders x 11 windows x 4 smoothers) are stored in the analysis data base for each realization. Figure 1 shows an example of the results from an analysis of the maximum-leakage simulation using the quadratic detrender, a 30% cosine window, and a 3-point smoother. The upper plot shows the difference between the measured slope (q) and the q value used to generate the data set (q_o), and the lower plot is the log-difference between the measured strength (T_1) and the T_1 value used in the generation (10^{16}). Both are plotted as a function of q_o.

The effects of windowing and smoothing on the analysis of the maximum-leakage simulation data set can be seen in Figure 2. These plots show the variation of Δq ($q - q_o$) and $\Delta \log$ (T_1) - 16.0) as a function of percent window taper for the non-smoothed case and for each of the four smoothers. The low-frequency terms were added to all data sets, and all were detrended using a quadratic detrender. Each data point is the average from all 66 realizations for that parameter and processing case. The most striking effect shown in these plots is the systematic loss in spectral power (as measured by T_1) caused by windowing the data and the recovery of this loss via the smoothing

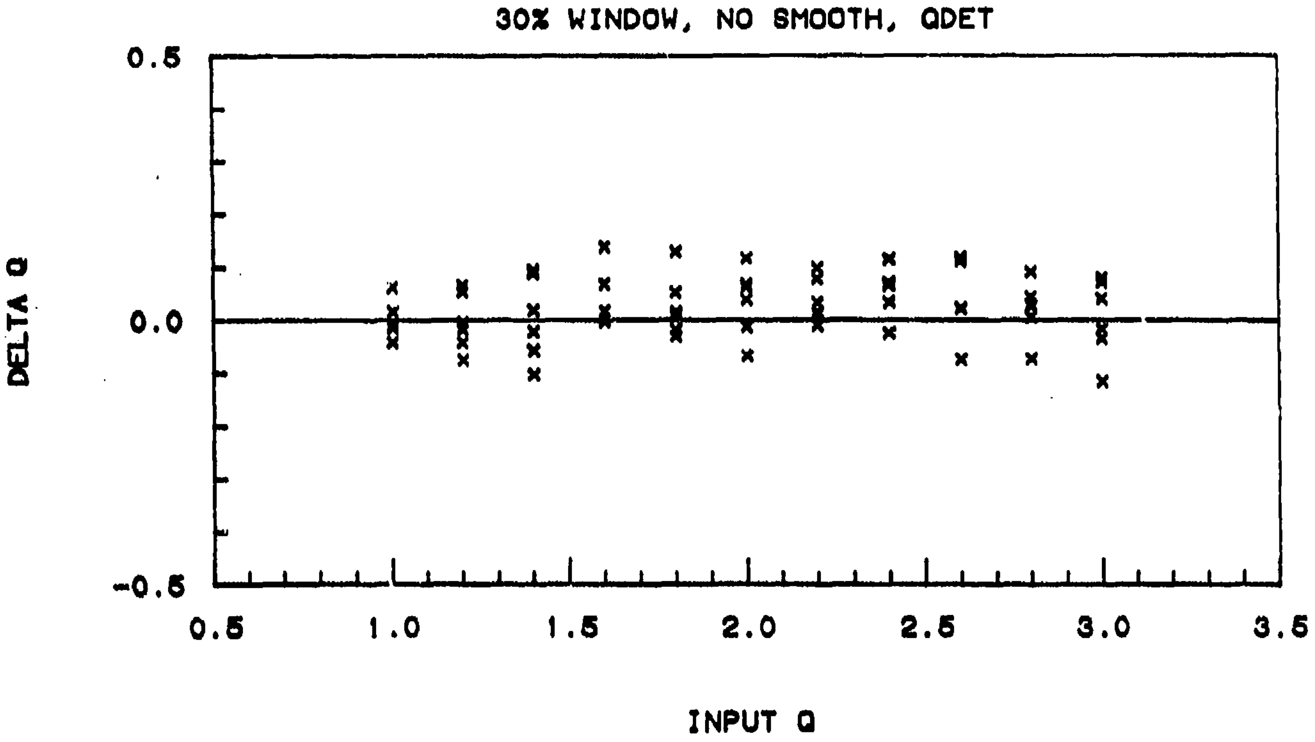

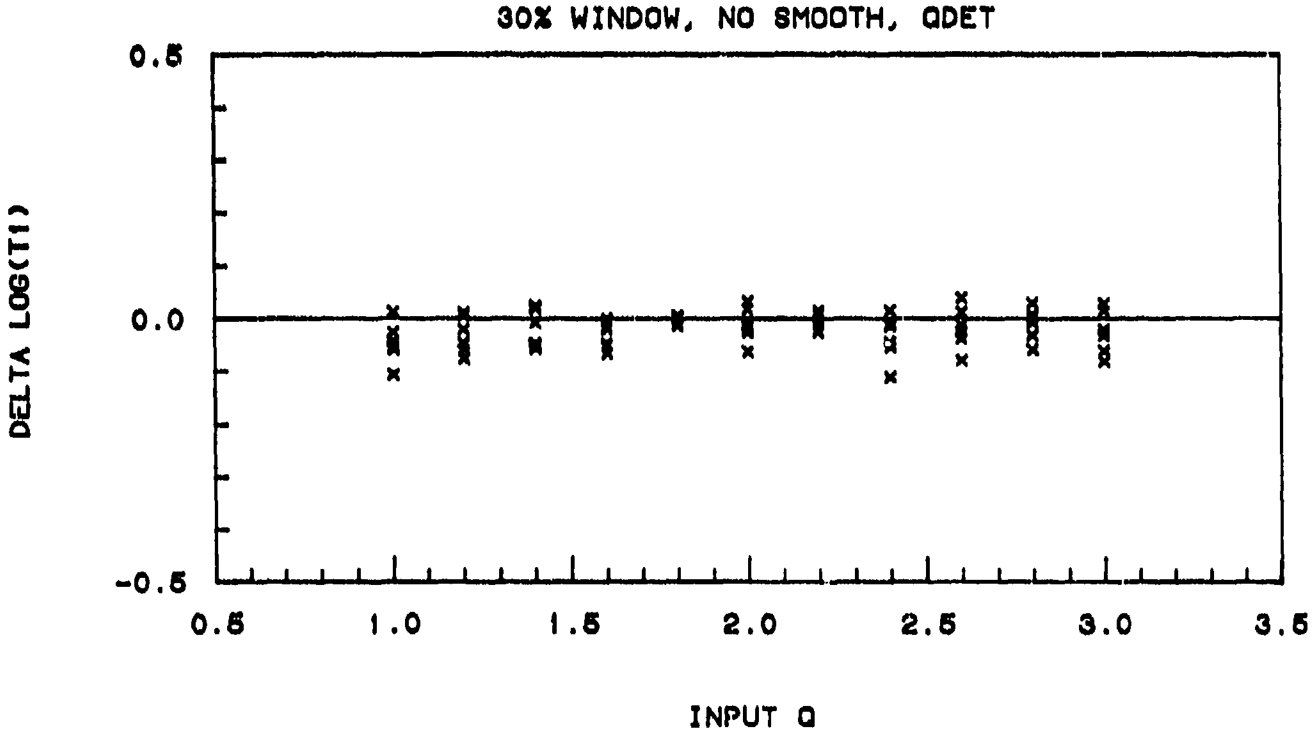

Figure 1. Sample analysis results for quadratic detrend, 30% window, and 3-point smoothing.

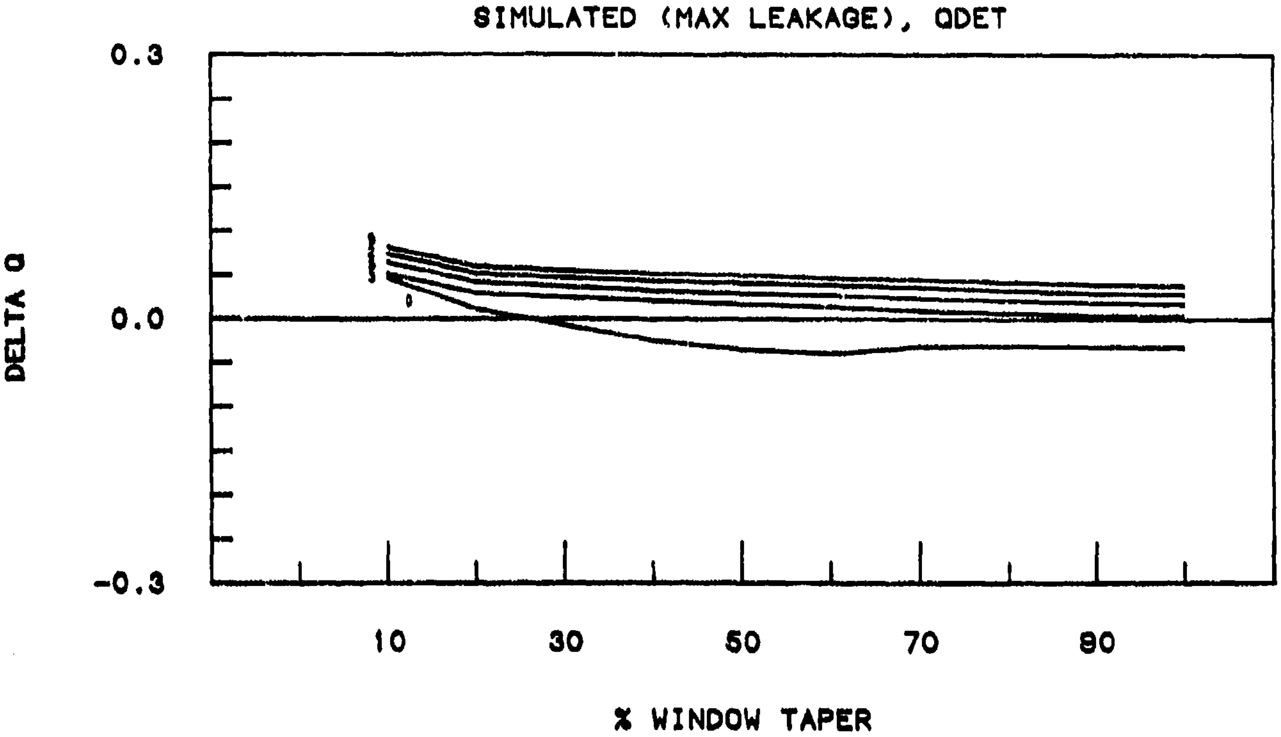

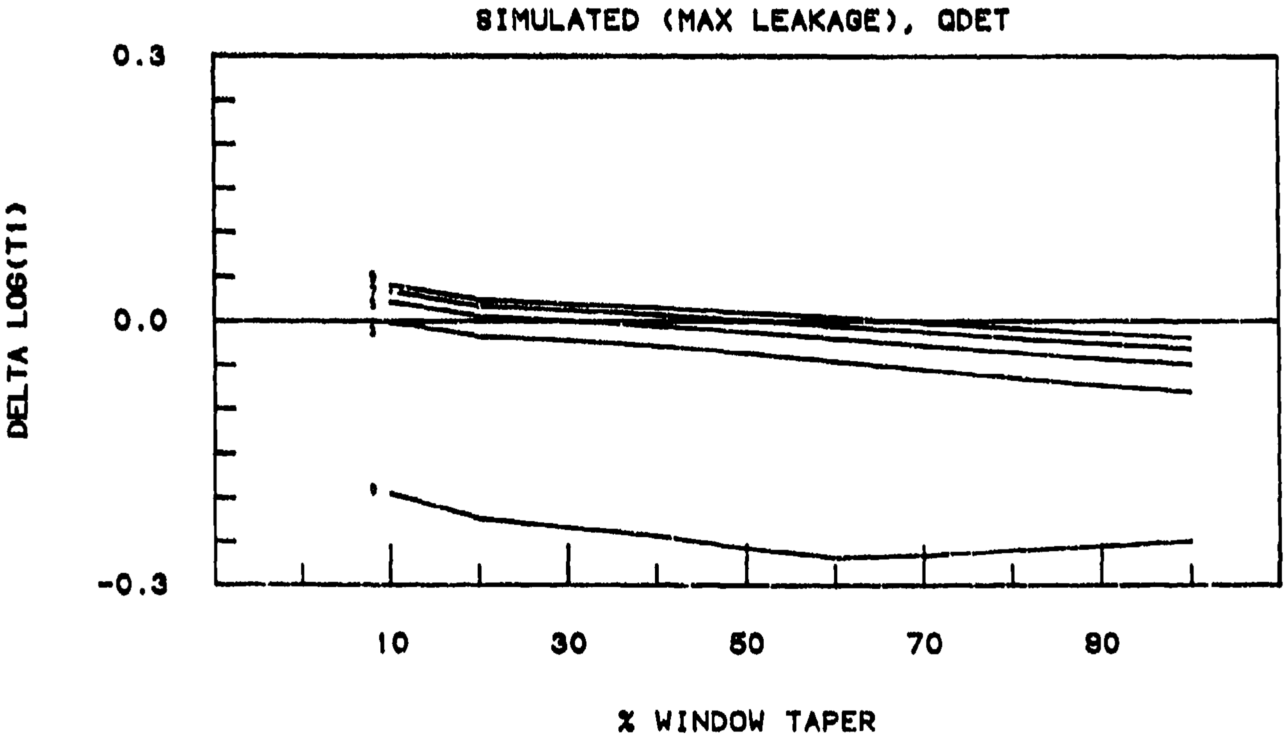

Figure 2. Effects of windowing and smoothing on data from the maximum-leakage simulation. All data sets were detrended with a quadratic detrender. Numbers indicate the number of points in the smoother.

process. It was expected that the effects of windowing and spectral smoothing would be inter-related, as windowing in the time domain is equivalent to smoothing in the frequency domain, but the loss of accuracy in T_1 due to windowing and the gain due to smoothing was completely unexpected. There is also a gain in terms of reduction of variance due to the smoothing. Figures 3 and 4 show the variation of Δq and $\Delta \log(T_1)$ for the unsmoothed and the smoothed (3-point smoother) cases. The vertical bars indicate the standard deviation (σ) of the 66 analyses in each case. The variance (σ^2) within all cases has been reduced by roughly a factor of four for both Δq and $\Delta \log (T_1)$. (Note: This analysis was repeated using the linear and end-match/mean-remove detrenders with the same results.)

Aside from this result, the general effect of increased severity in the window was to decrease (though not necessarily improve) both Δq and $\Delta \log(T_1)$, and the general effect of smoothing was to increase (though not necessarily worsen) both. The selection of an optimal choice of window severity and smoother size came down to a trade-off between accuracy of reproducing q or T_1. The final selection was to use a 30% cosine window and a 5-point smoother. Figure 5 is a similar plot to Figure 4 for the 5-point smoother showing the standard deviations for this case.

Figure 6 indicates the effects of the three detrenders used in these tests. In both plots, the upper curve (labeled L) is from the linear detrend, the next down is from the end-match/mean-remove detrend (E), and the lower curve from the quadratic detrend (Q). As can be seen, there is little difference between the three, particularly for the more severe windows. For the 30% window, the quadratic detrend case is slightly better that the other two, and the variance is also slightly better for the quadratic detrend.

The main difficulty in performing a similar analysis of the results of processing the Wideband data sample is in determining what "truth" is in terms of q and T_1 for each 512-point data set. For the purposes of this study, it was decided to define truth as the results obtained from the processing procedure selected in the simulation

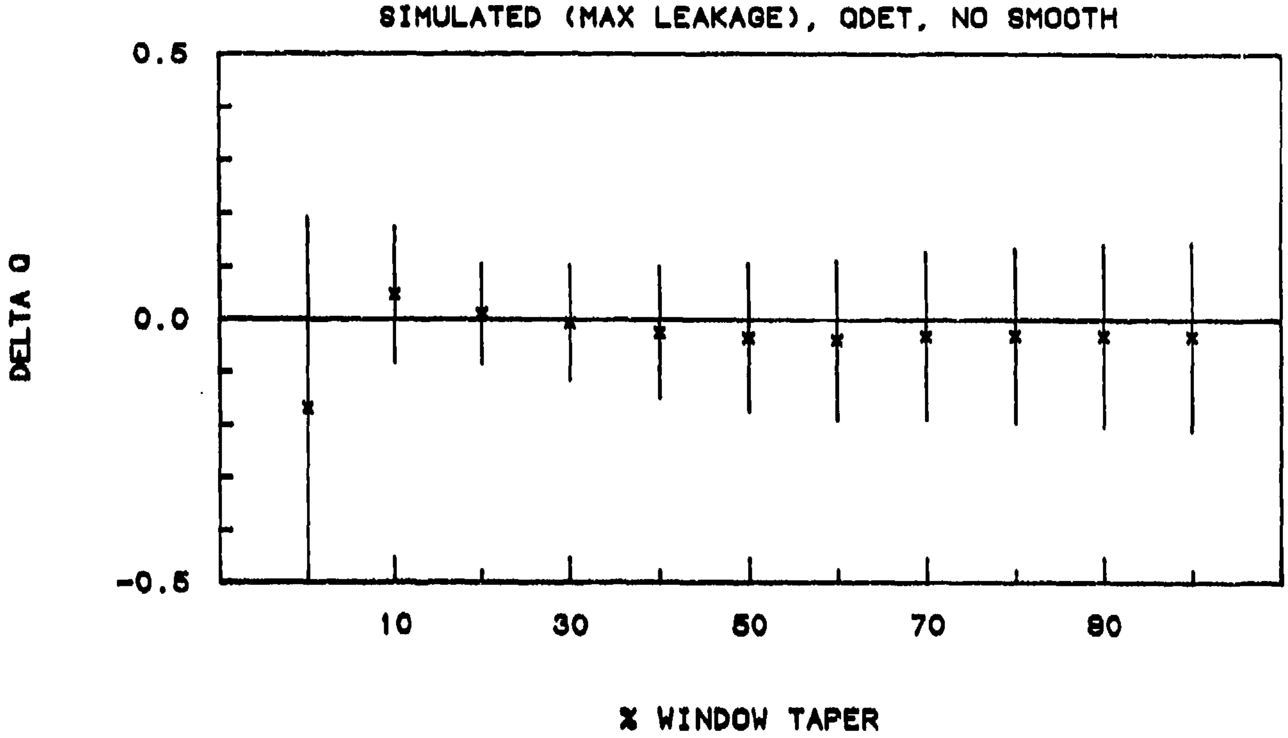

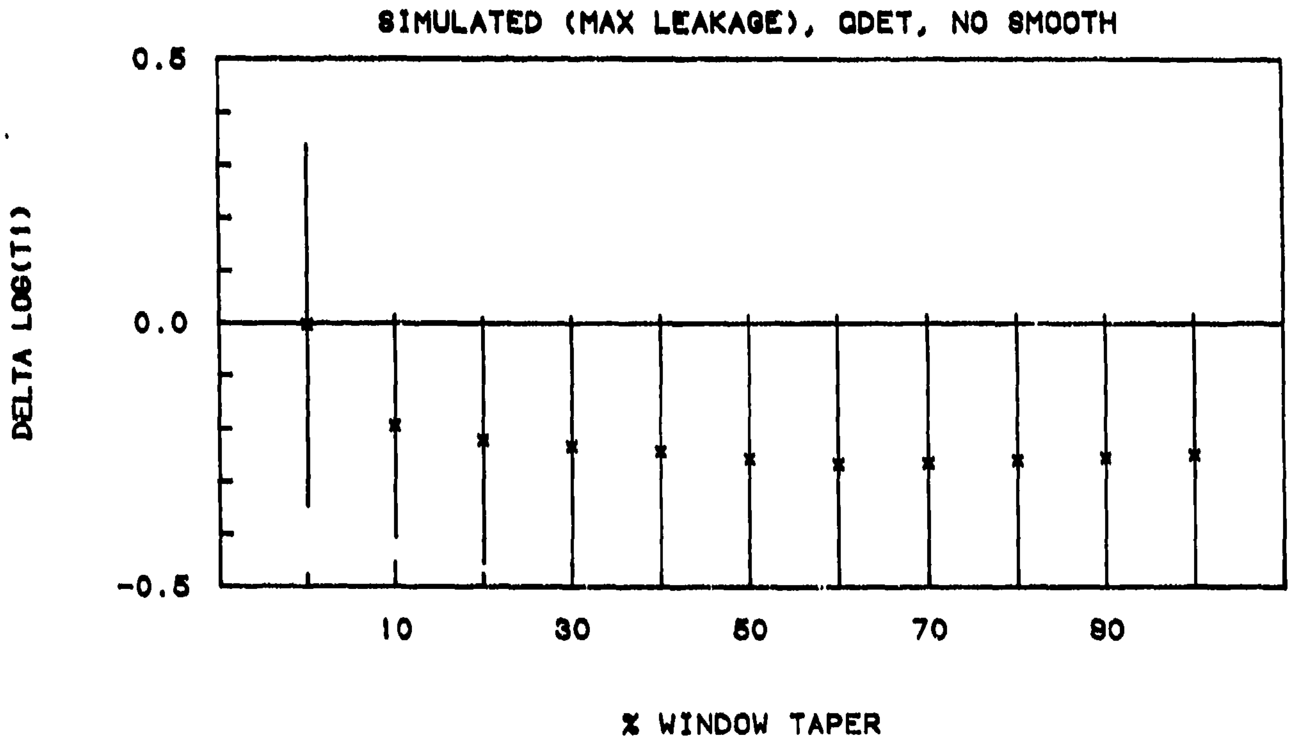

Figure 3. Mean and standard deviation variation with window severity for non-smoothed case.

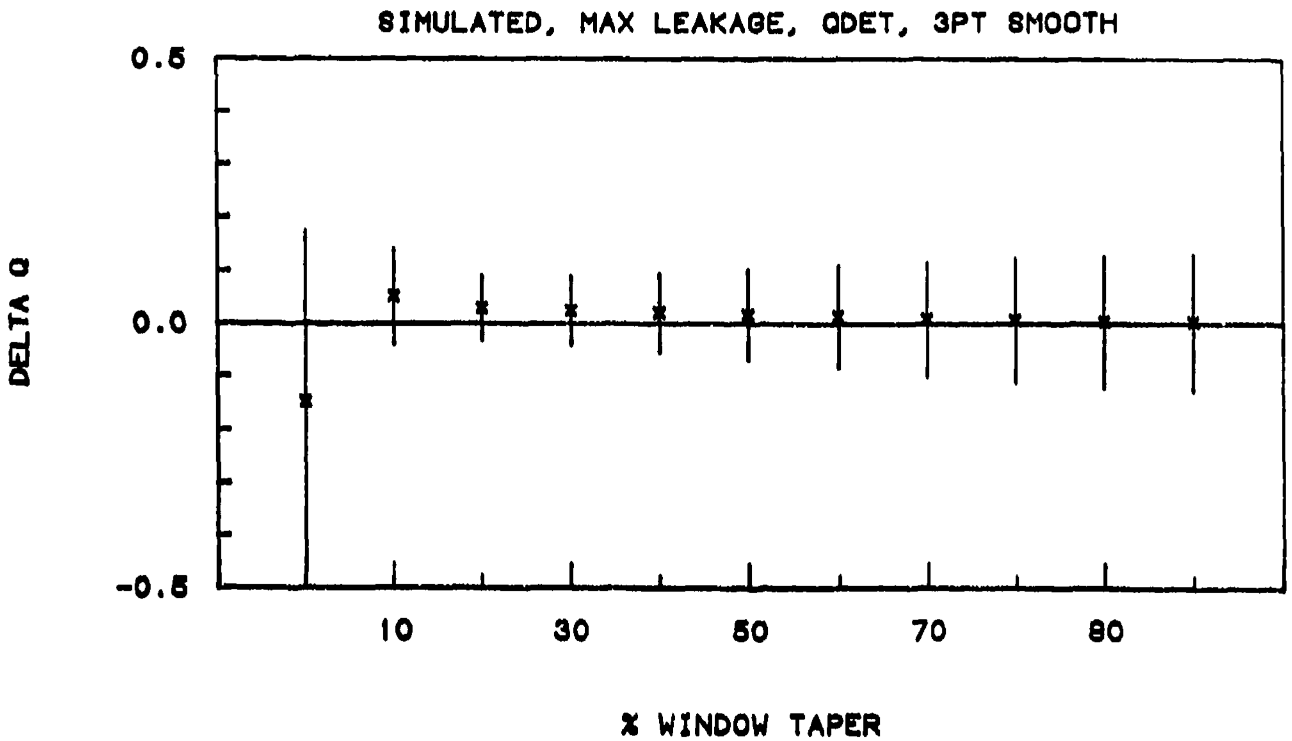

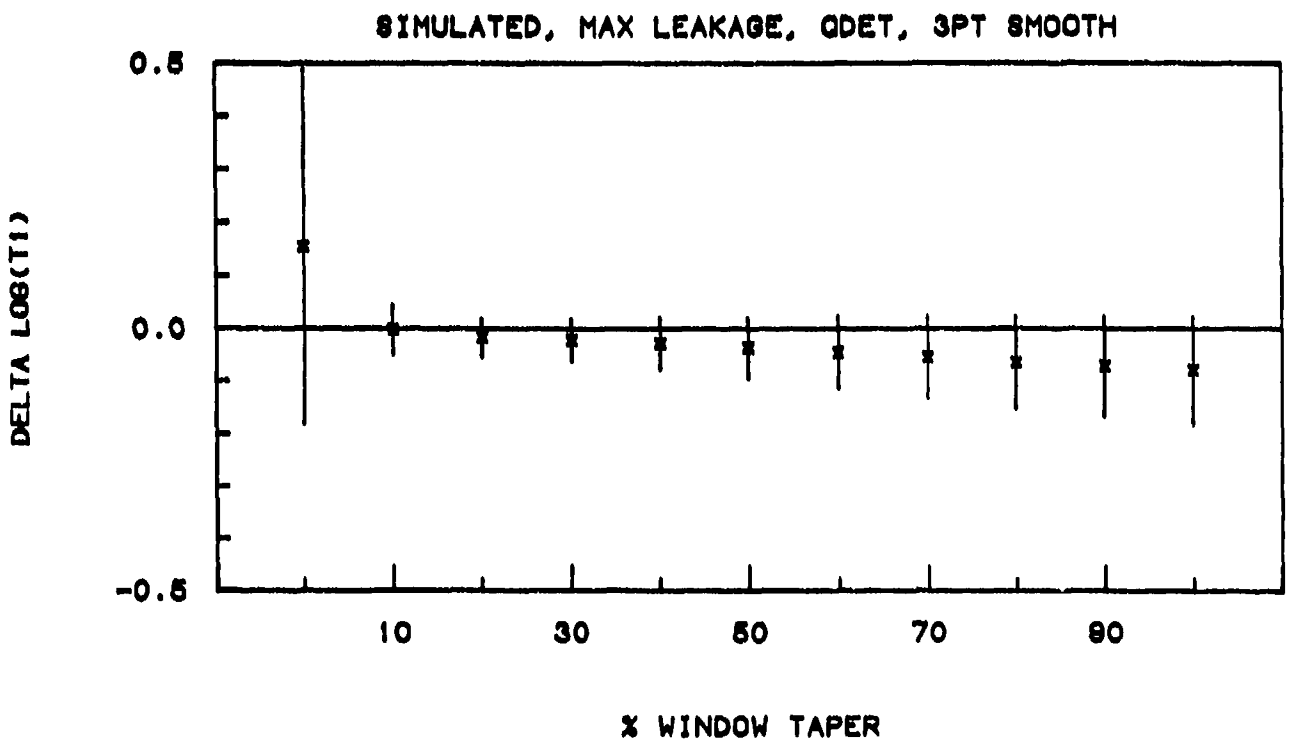

Figure 4. Mean and standard deviation variation with window severity for 3-point smoother case.

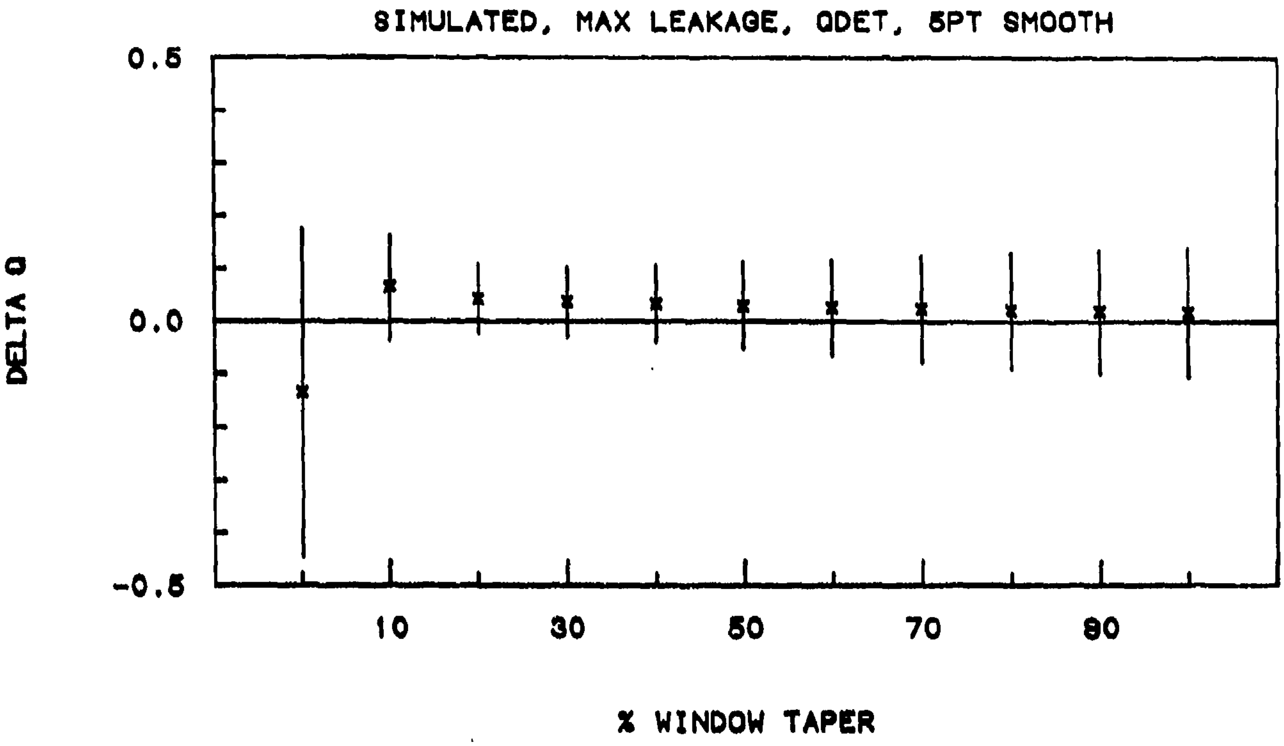

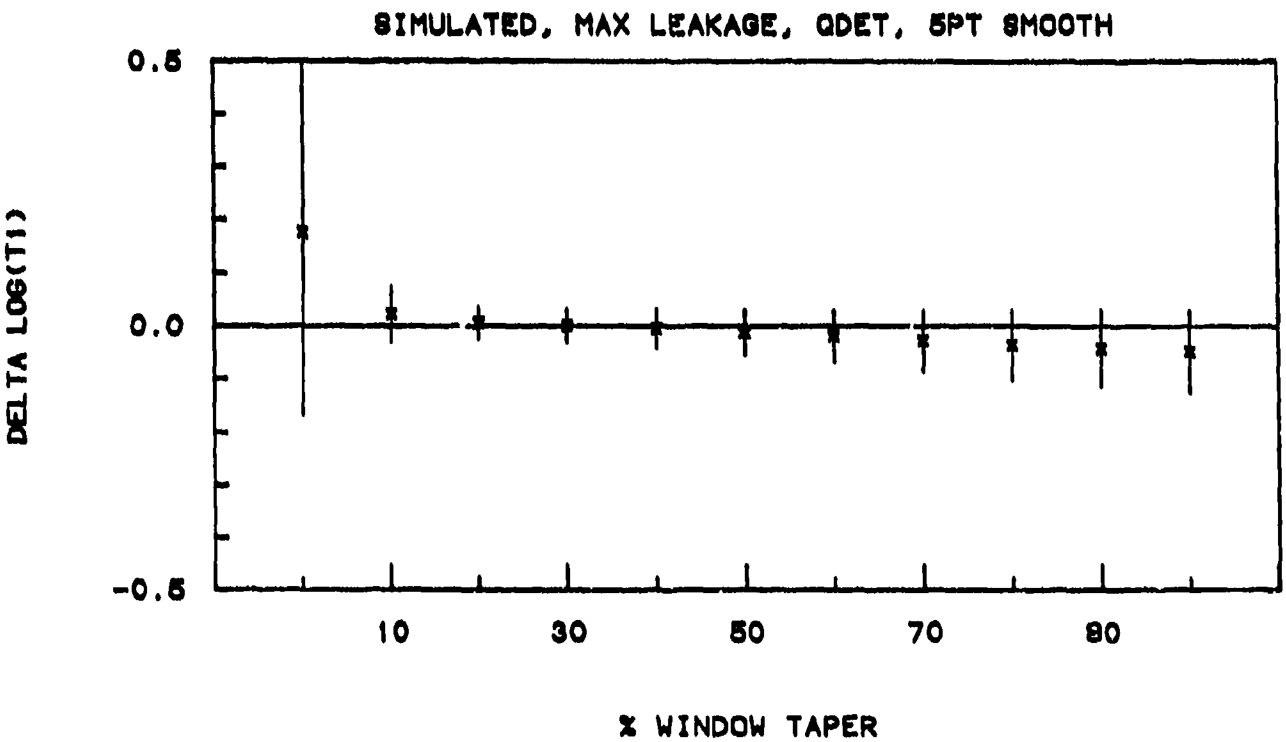

Figure 5. Mean and standard deviation variation with window severity for 5-point smoother case.

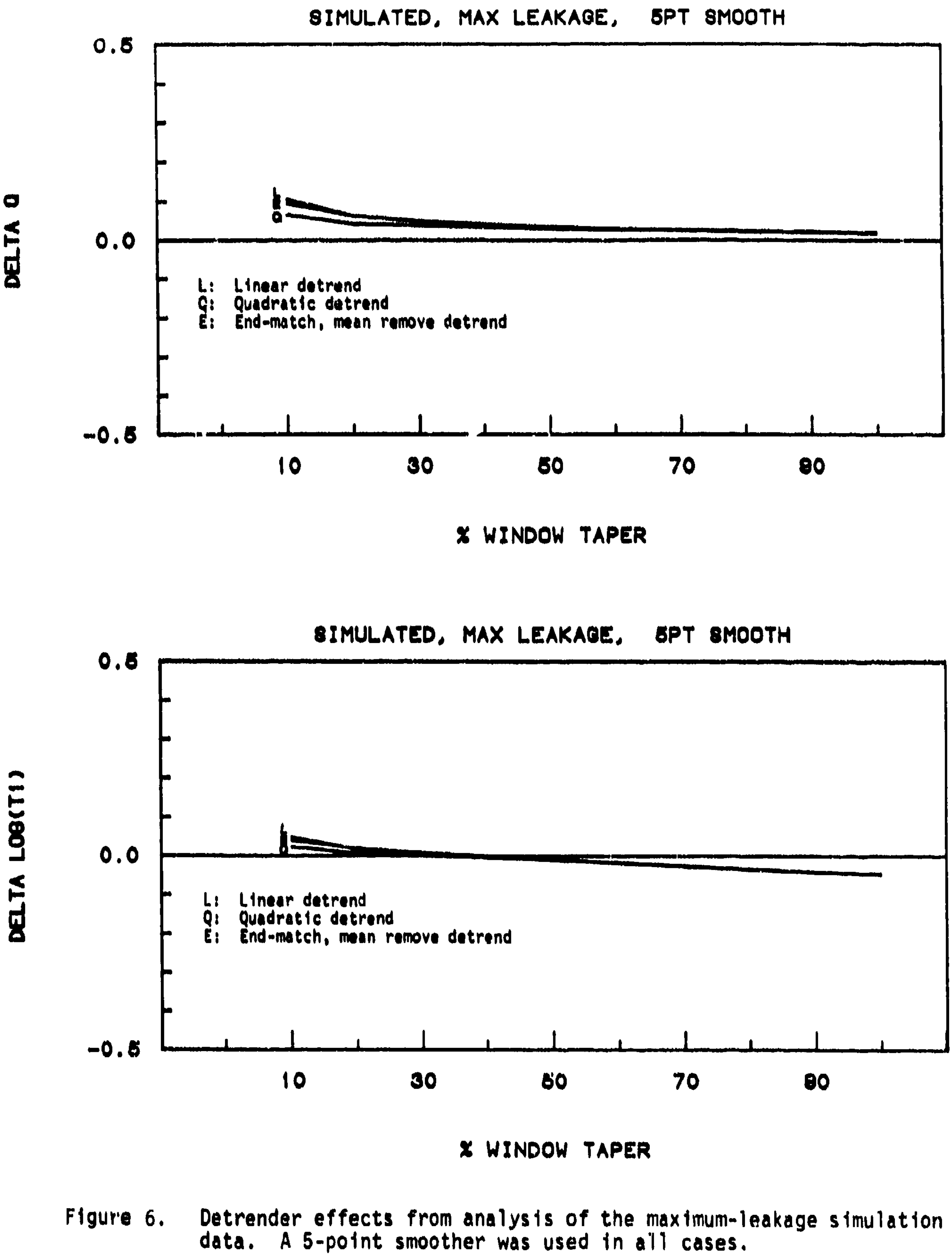

Figure 6. Detrender effects from analysis of the maximum-leakage simulation data. A 5-point smoother was used in all cases.

study (quadratic detrend, 30% cosine window, 5-point smoother) and use these values for calculating Δq and $\Delta \log(T_1)$. This will at least show whether the general effects found in the simulation study are also true for the observed data set.

Figure 7 shows plots of Δq and $\Delta \log(T_1)$ as functions of window severity for each of the five smoothing cases for pass PF-52-47. The same behavior is found in these plots as in Figure 2 for the simulated data set, i.e., the loss/gain in $\Delta \log(T_1)$ due to windowing/smoothing, and the trends in Δq and $\Delta \log(T_1)$ as functions of window severity and smoother size. Note that both curves pass through zero for the 30% cosine window and 5-point smoother as this was defined as "truth." The variances for each data point for the various cases were also similar to those from the simulated data set, although they were more strongly a function of window and smoothing, since the base values of q and $\log(T_1)$ were defined in terms of the output from one of the processing methods.

The results of the detrender study for this data set are presented in Figure 8. The fourth curve on these plots, labeled F, is the results obtained using the low-pass filter detrender used in generating the phase plots in Figure A-4. Since the quadratic detrender was used in defining the base analysis values, the results from these plots do not necessarily indicate that the quadratic detrend results (curve Q) are better than those from the low-pass filter detrend, but they do indicate that the two methods provide essentially the same results.

Based on the results of processing both the simulated and observed data sets, the processing method to be used in calculating estimates of q and T_1 from the DMSP SSIES data sets is as follows:

1. Detrend each 512-point data set by removing the quadratic trend determined by a least-squares fit to the data set.

2. Window the detrended data using a 30% split-bell cosine window.

3. Calculate an estimate of the PDS from an FFT of the windowed, detrended data set.

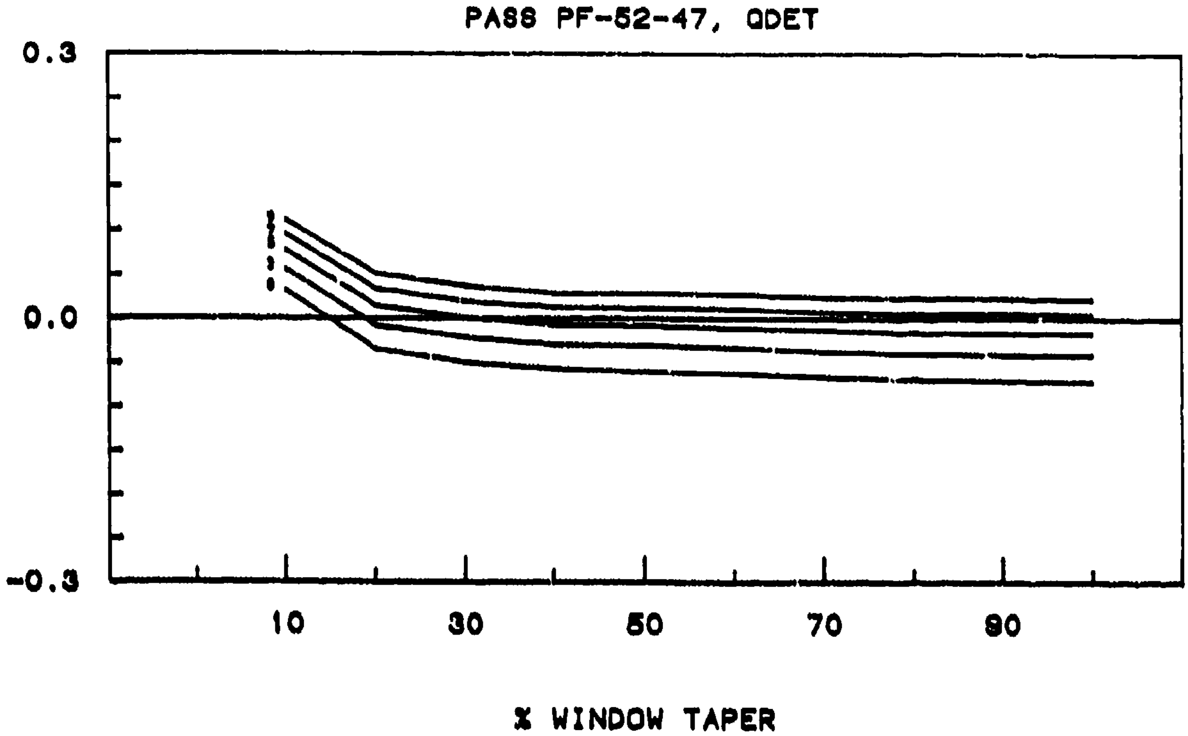

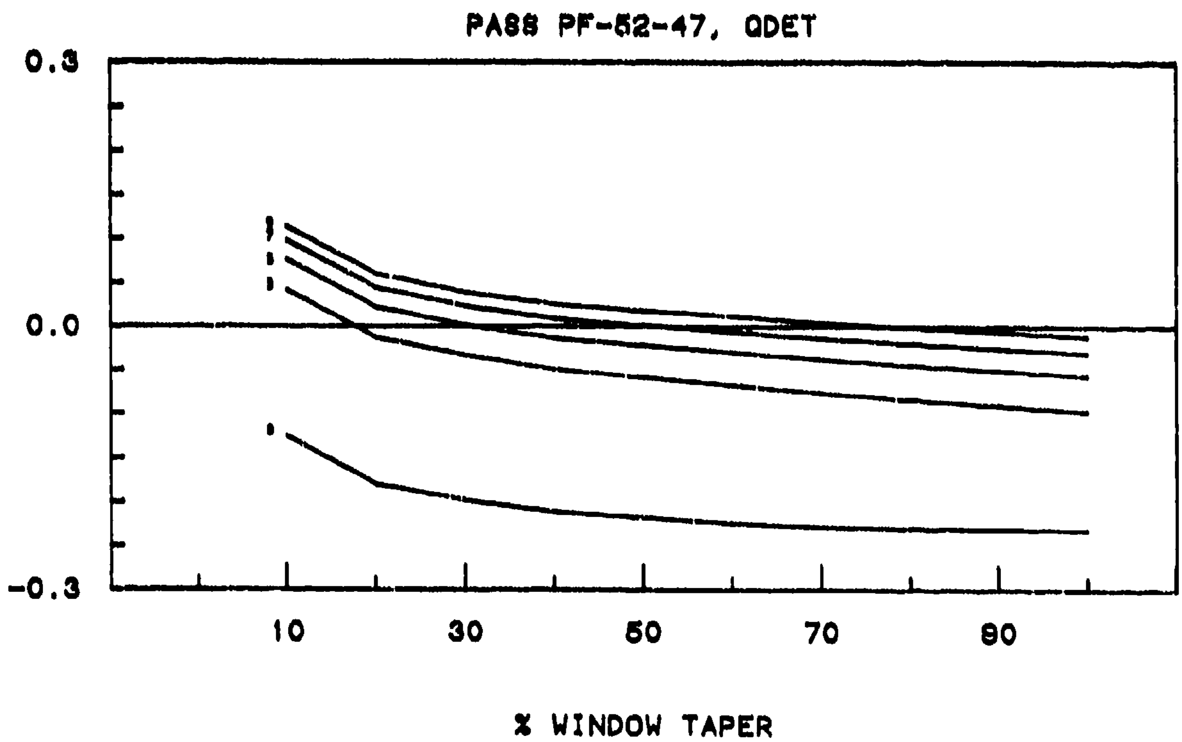

Figure 7. Effects of windows and smoothing on data from pass PF-52-47. All data sets were detrended using a quadratic detrender. Numbers indicate number of points in smoother.

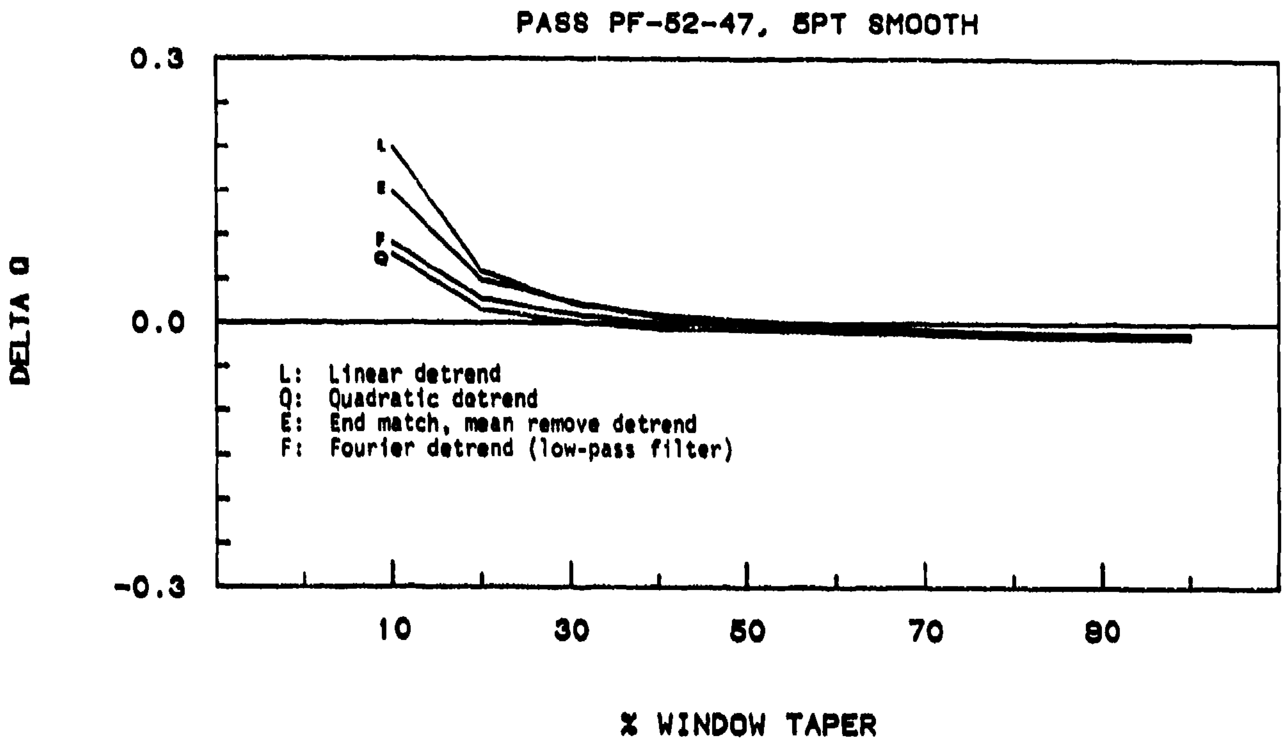

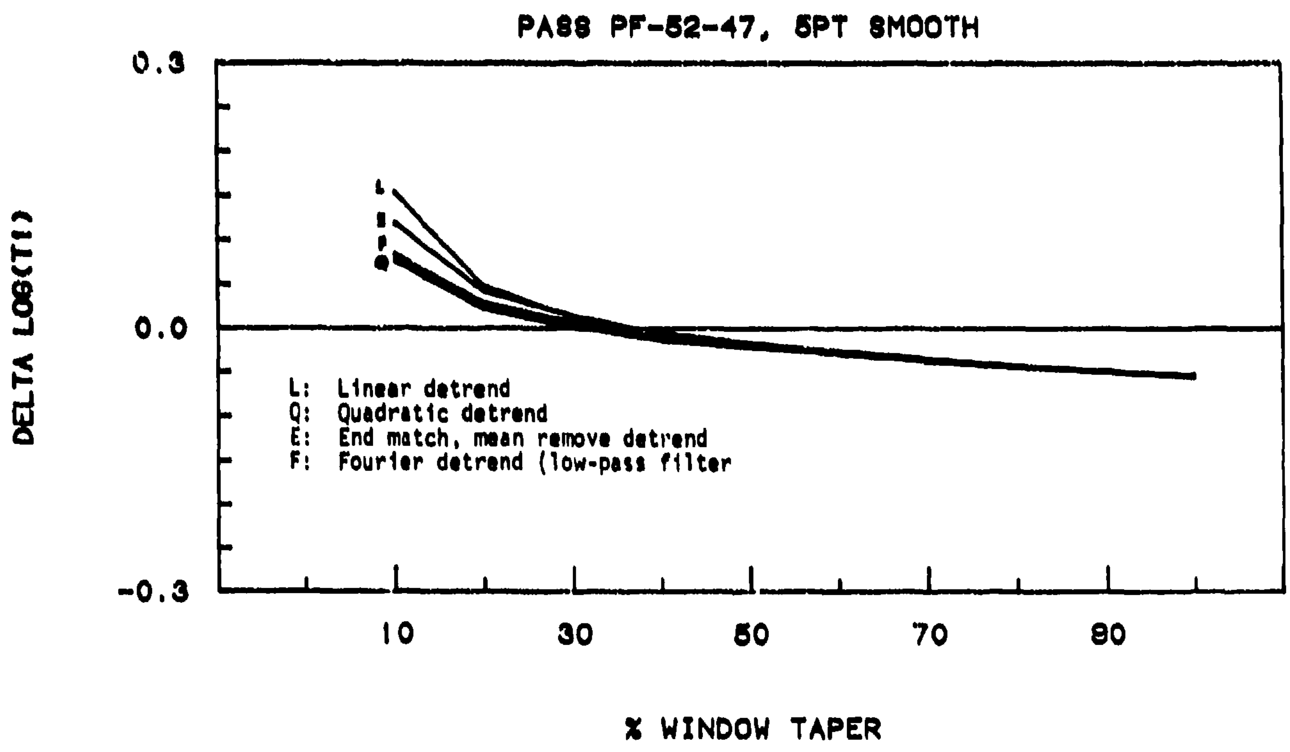

Figure 8. Detrender effects from analysis of data from pass PF-52-47. A 5-point smoother was used in all cases.

4. Smooth the PDS estimate using a 5-point, centered smoother with binomial weights.

5. Calculate estimates of q and T_1 from a log-linear fit to the smoothed PDS over the frequency range 0.2 to 7.0 Hz.

The above processing was performed on the two simulated data sets, each containing 66 data samples, and on a third data set containing 60 data samples equally divided among q values of 1.0, 2.0, and 3.0. The RMS error in q for the 192 samples was 3.3% and the error in T_1 was 6.7%. Table 1 shows the variation of ΔC_k (%) with q and v_p calculated using Equation [1] with these percent RMS errors in q and T_1. The ΔC_k values in the bottom row are weighted RMS values for each v_p calculated using the weights listed in the rightmost column. These weights are generated from a gaussian function centered at q = 1.8 with a 1/e-width of 0.6. This is done to simulate the expected distribution of q, and was taken from analyses of phase scintillation data collected from the DNA HiLat satellite. The expected errors in C_k due to errors in the estimates of q and T_1 range from roughly 7% at low values of v_p to roughly 10% for high values.

3.3 Uncertainties in C_k Calculated from $\langle \Delta N_e^2 \rangle$

The alternative method for calculating an estimate of C_k from a plasma density sample, employed in cases where the PDS is not calculated from the density samples, uses the density variance, $\langle \Delta N^2 \rangle$. The estimate of C_k is calculated using an Equation [3] in which q, the PDS power-law slope, is not observed but rather set to some median value. As the shape of the underlying PDS for ionospheric density irregularities is a red power-law, the variance for a given data sample is very strongly dependent on both the slope of the PDS and the effects of detrending reflected in the cutoff frequency, f_c. The purpose of the parametric study for this method is to determine the magnitude of inaccuracies introduced in C_k calculated using Equation [3] due to uncertainties in the values used for f_c and q.

TABLE 1. Variation of ΔC_k (%) with q and v_p for Δq = 3.3% and ΔT_1 = 6.7%. Bottom line is the weighted RMS ΔC_k for all q as a function of v_p.

q	Δq				ΔC_k				Weight
		1000.	2000.	3000.	4000.	5000.	6000.	7000.	
1.2	0.04	6.1	5.5	5.5	5.8	6.0	6.3	6.6	0.3679
1.3	0.04	6.1	5.5	5.6	5.9	6.2	6.5	6.9	0.4994
1.4	0.05	6.1	5.5	5.7	6.0	6.4	6.8	7.2	0.6412
1.5	0.05	6.1	5.5	5.7	6.2	6.7	7.1	7.5	0.7788
1.6	0.05	6.1	5.5	5.8	6.4	6.9	7.4	7.9	0.8948
1.7	0.06	6.1	5.5	5.9	6.6	7.2	7.8	8.3	0.9726
1.8	0.06	6.1	5.5	6.1	6.8	7.5	8.1	8.7	1.0000
1.9	0.06	6.1	5.5	6.2	7.0	7.8	8.5	9.1	0.9726
2.0	0.07	6.1	5.6	6.4	7.3	8.1	8.9	9.5	0.8948
2.1	0.07	6.1	5.6	6.5	7.5	8.4	9.3	10.0	0.7788
2.2	0.07	6.1	5.6	6.7	7.8	8.8	9.7	10.4	0.6412
2.3	0.08	6.1	5.7	6.8	8.1	9.1	10.1	10.9	0.4994
2.4	0.08	6.1	5.8	7.0	8.3	9.5	10.5	11.4	0.3679
		6.1	5.5	6.1	6.9	7.6	8.3	8.9	RMS ΔC_k

Estimates for f_c and the uncertainty in this parameter for the quadratic, linear, and end-match detrenders were obtained by calculating an effective f_c, defined by

$$f_{ce} = \left[\frac{2T_1}{(q-1)\langle \Delta N^2 \rangle} \right]^{1/(q-1)} \qquad [4]$$

for each simulated realization and calculating the mean and variance of the values obtained for each detrender. This provided the following results:

Quadratic detrend: $f_c = 0.06 \pm\text{-}25\%$
Linear detrend: $f_c = 0.04 \pm\text{-}45\%$
End-match/mean remove: $f_c = 0.03 \pm\text{-}50\%$.

The value of f_c for the low-pass filter detrender is essentially determined by the cutoff frequency specified in constructing the filter. For the sake of this study, we will define the detrender cutoff frequency such that the detrend period, which is the reciprocal of this frequency, is roughly one-half the sample interval. Since the simulation data are set up to be 24 samples/second and the sample size is 512 data points, the sample interval is 21.333... seconds. For convenience, we will select a 10-second detrend interval which provides $f_c = 0.10$. It was difficult to determine a variance in f_c for this detrender using the simulated data sets because these data were constructed in such a way that the power is located at discrete frequencies rather than spread across all frequencies. In the tests run, however, the largest variances found were on the order of 3-4%.

An initially attractive feature of this method for calculating C_k is that one need not calculate the PDS of the data sample if a mean value of the PDS slope, q, could be used. In early simulations, however, it became apparent that this could not be done. Even for the best cases, assuming no error in f_c or any other parameters, the minimum RMS errors in C_k were on the order of 50%. The RMS error increased to over 100% when realistic values for expected errors in other parameters were used. It was decided, therefore, to assess the level of errors to be expected from this method assuming that q is measured with a level of accuracy established in earlier studies ($\pm$3.3%).

Tables 2a-c summarize the expected errors in C_k using Equation 2 for the Fourier detrender (f_c = 0.10, Δf_c = 3.5%), the quadratic detrender (f_c = 0.06, Δf_c = 25%), and the linear and end-match detrenders (f_c = 0.35, Δf_c = 45%). The errors for the Fourier detrender are comparable to those found for the C_k calculation method using q and T_1 shown in Table 1, while the levels for the quadratic and linear detrenders are factors of 2 and 4 larger, respectively. [Note: As with the results reported earlier for q and T_1, these tables do not include the effects of expected errors in v_p.] The large errors in the quadratic and linear detrender cases, reflected in the large variances in the effective values for f_c, are due to the data-dependent nature of the effects of these detrenders on the large-scale features which dominate $\langle \Delta N^2 \rangle$. In other words, the amount of low-frequency power removed in the detrending process will depend on the location of the extrema of the large-scale features in the data sample. The Fourier detrender, which must be run on the entire data set prior to selecting 512-point data samples for processing, is designed to remove power only at frequencies below the specified cutoff frequency and is not affected by the location of the extrema.

In summary, if this method is to be used for calculating C_k, the following rules should be followed:

a. The data should be detrended using a detrender which will remove power at the larger scales in a predictable manner, such as the Fourier detrender used in this study.

b. A power-density spectrum (PDS) should be constructed from each data sample as described in Section 4.1 to obtain an estimate of the spectral slope rather than using a mean value for q.

If the data are processed in this fashion, the expected errors in C_k for this technique due to uncertainties in f_c and q will be roughly 6-9% for low values of v_p and 12% for high values.

TABLE 2a. Variation of ΔC_k (%) with q and v_p for the Fourier detrender (f_c=0.10, Δf_c=3.5%) using Δq = 3.3%. The bottom line is the weighted RMS ΔC_k for all q as a function of v_p.

q	Δq	ΔC_k 1000.	2000.	3000.	4000.	5000.	6000.	7000.	Weight
1.2	0.04	11.5	9.3	8.1	7.2	6.5	5.9	5.5	0.3679
1.3	0.04	6.4	4.1	2.8	1.9	1.4	1.2	1.3	0.4994
1.4	0.05	3.7	1.6	1.4	2.2	2.9	3.5	4.0	0.6412
1.5	0.05	2.1	2.0	3.3	4.3	5.2	5.9	6.5	0.7788
1.6	0.05	1.8	3.5	5.0	6.2	7.1	7.9	8.6	0.8948
1.7	0.06	2.4	4.9	6.6	7.9	8.9	9.7	10.4	0.9726
1.8	0.06	3.3	6.2	8.0	9.4	10.5	11.3	12.1	1.0000
1.9	0.06	4.2	7.4	9.4	10.8	11.9	12.9	13.6	0.9726
2.0	0.07	5.2	8.5	10.6	12.2	13.3	14.3	15.2	0.8948
2.1	0.07	6.0	9.6	11.8	13.4	14.7	15.7	16.6	0.7788
2.2	0.07	6.9	10.7	13.0	14.7	16.0	17.1	18.1	0.6412
2.3	0.08	7.7	11.7	14.2	15.9	17.3	18.5	19.5	0.4994
2.4	0.08	8.6	12.7	15.3	17.2	18.6	19.8	20.9	0.3679
		5.3	7.4	9.0	10.3	11.3	12.1	12.8	RMS ΔC_k

TABLE 2b. Variation of ΔC_k (%) with q and v_p for the quadratic detrender (f_c=0.06, Δf_c=25%) using Δq = 3.3%. The bottom line is the weighted RMS ΔC_k for all q as a function of v_p.

q	Δq	ΔC_k 1000.	2000.	3000.	4000.	5000.	6000.	7000.	Weight
1.2	0.04	10.7	8.8	7.7	7.0	6.5	6.1	5.8	0.3679
1.3	0.04	7.8	6.7	6.4	6.3	6.4	6.5	6.7	0.4994
1.4	0.05	8.5	8.4	8.7	9.0	9.4	9.7	10.0	0.6412
1.5	0.05	10.3	10.8	11.4	11.9	12.4	12.8	13.2	0.7788
1.6	0.05	12.5	13.3	14.1	14.7	15.3	15.7	16.2	0.8948
1.7	0.06	14.7	15.8	16.7	17.4	18.0	18.5	19.0	0.9726
1.8	0.06	17.0	18.2	19.2	20.0	20.7	21.2	21.7	1.0000
1.9	0.06	19.3	20.6	21.7	22.6	23.3	23.9	24.4	0.9726
2.0	0.07	21.5	23.0	24.2	25.1	25.9	26.6	27.1	0.8948
2.1	0.07	23.8	25.4	26.7	27.7	28.5	29.2	29.8	0.7788
2.2	0.07	26.0	27.8	29.2	30.2	31.1	31.9	32.5	0.6412
2.3	0.08	28.3	30.3	31.7	32.8	33.8	34.6	35.3	0.4994
2.4	0.08	30.6	32.7	34.2	35.5	36.5	37.3	38.1	0.3679
		18.6	19.8	20.8	21.6	22.2	22.8	23.3	RMS ΔC_k

TABLE 2c. Variation of ΔC_k (%) with q and v_p for the linear detrenders (f_c=0.035, Δf_c=45%) using Δq = 3.3%. The bottom line is the weighted RMS ΔC_k for all q as a function of v_p.

q	Δq	ΔC_k							Weight
		1000.	2000.	3000.	4000.	5000.	6000.	7000.	
1.2	0.04	11.5	10.1	9.4	9.0	8.8	8.6	8.5	0.3679
1.3	0.04	12.1	11.8	11.8	11.9	12.1	12.2	12.4	0.4994
1.4	0.05	15.4	15.6	16.0	16.3	16.6	16.8	17.1	0.6412
1.5	0.05	19.2	19.7	20.2	20.6	20.9	21.3	21.5	0.7788
1.6	0.05	22.9	23.6	24.2	24.7	25.1	25.5	25.8	0.8948
1.7	0.06	26.7	27.6	28.2	28.8	29.3	29.7	30.0	0.9726
1.8	0.06	30.4	31.4	32.2	32.8	33.4	33.8	34.2	1.0000
1.9	0.06	34.2	35.3	36.2	36.9	37.5	38.0	38.4	0.9726
2.0	0.07	37.9	39.2	40.2	41.0	41.6	42.2	42.7	0.8948
2.1	0.07	41.7	43.2	44.3	45.1	45.8	46.4	47.0	0.7788
2.2	0.07	45.6	47.2	48.4	49.4	50.1	50.8	51.4	0.6412
2.3	0.08	49.5	51.4	52.7	53.7	54.6	55.3	56.0	0.4994
2.4	0.08	53.6	55.6	57.0	58.2	59.1	60.0	60.7	0.3679
		32.9	33.9	34.8	35.4	36.0	36.5	36.9	RMS ΔC_k

3.4 Uncertainties in C_k Due to Uncertainties in v_p

The final part of this parametric study is aimed at determining the expected errors in estimating v_p and the effects of these errors on estimates of C_k. This parameter is a function of (1) the satellite velocity vector, which is well determined; (2) the orientation of the geomagnetic field at the satellite, which can be fairly well determined from standard models of the geomagnetic field, (3) the velocity of the irregularities with respect to the satellite, which can be measured or taken from a model; and (4) the axial ratios of the irregularities and their orientation with respect to the geomagnetic field, which cannot be extracted from the satellite data set and must be obtained from models which are still in their early evolutionary stages. This study will focus on the effects of errors in the measured/modeled drift velocity and in the modeled axial ratios on v_p, and the effects of these errors on C_k.

Figure 9 is a scatter plot of v_p vs. apex (magnetic) latitude calculated for 28 simulated DMSP orbits, 14 of them with the local time of ascending node at 0600 and 14 at 1000. The IGRF80 model was used to obtain parameters pertaining to the the geomagnetic field, and modified WBMOD models were used for the axial ratios (a and b) and the *in situ* drift velocity. The pattern in this plot is a function of the orientation of the DMSP orbit with respect to the geomagnetic field and the orientation and axial ratios of the irregularities. In the equatorial region, the velocities are low because (1) the angle between the orbital plane and the geomagnetic field direction is small and (2) the irregularities in the equatorial region are elongated rods aligned with the geomagnetic field direction. Thus the satellite is moving along the long axis of the irregularities, resulting in a low v_p. The increase in v_p with apex latitude is due primarily to the changing angle between the satellite velocity vector and the geomagnetic field vector. The sudden "spreading" of the v_p curve at high latitudes is due to (1) the addition of an appreciable *in situ* drift velocity as the satellite enters the high-latitude convection

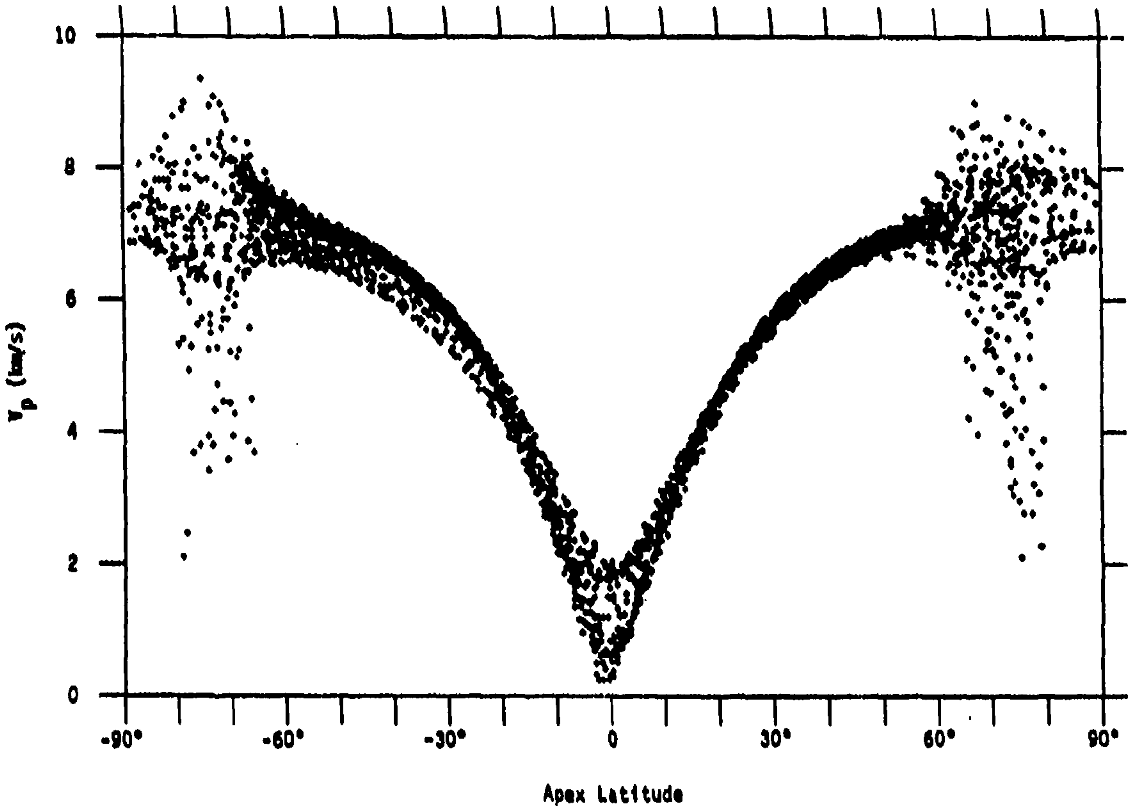

Figure 9. Scatter plot of the parameter V_p as a function of apex latitude for 14 dawn-dusk and 14 noon-midnight DMSP orbits.

pattern and (2) the introduction of sheet-like irregularities ($b>1$) in certain sections of the auroral zone. [Note: In the model used for axial ratio b, sheet-like irregularities are confined to the evening side of the auroral oval (roughly 1800-2400 magnetic local time (MLT)).] As we shall see later, the effect of the sheet-like irregularities is to reduce the calculated v_p.

In order to estimate the effects of errors in a and b, v_p was calculated for the dawn-dusk (0600LT) cases used in generating Figure 9 with induced "errors" of $\pm$-50% in each axial ratio, and the percent error in v_p was calculated. The results are shown in the two scatter plots in Figure 10. As can be seen in the upper plot in this figure, v_p is very insensitive to errors in a except for a few cases near the magnetic equator. All but 3 of 1440 data points resulted in an error in v_p of less than 5%, and the maximum error in v_p was 26%. On the other hand, v_p can be very sensitive to errors in axial ratio b, as can be seen in the lower plot in Figure 10. [Note: Errors were introduced only in those cases where $b>1$, and b was not allowed to be less than 1.] The bulk of the errors is still below 5% (96% of the errors at all latitudes, and 88% of the errors for latitudes >60 degrees, were below 5%); however, the range in v_p errors is now -35% to +100%. Fortunately, the area where sheet-like irregularities exist appears to be limited to the evening-side auroral oval (Fremouw, private correspondence); unfortunately, this is an area of interest.

A second error which involves the axial ratios is specifying sheet-like irregularities where the irregularities are actually rod-like, and vice versa. Figure 11 is a scatter plot of v_p percent error for the same cases used in Figure 10 when b is set to 1.0 everywhere. The range of errors is now 0% to over 300%, with 95% of the total distribution, and 84% of the distribution at latitudes >60 degrees, with errors <5%. Figure 12 shows the effect of forcing rod-like irregularities everywhere on v_p. The upper plot shows v_p calculated using the model for b for the dawn-dusk orbits, and the lower plot shows v_p calculated for $b=1$. Removing the sheet like irregularities shifts all values of v_p above 6000 m/s. Again, the locations and

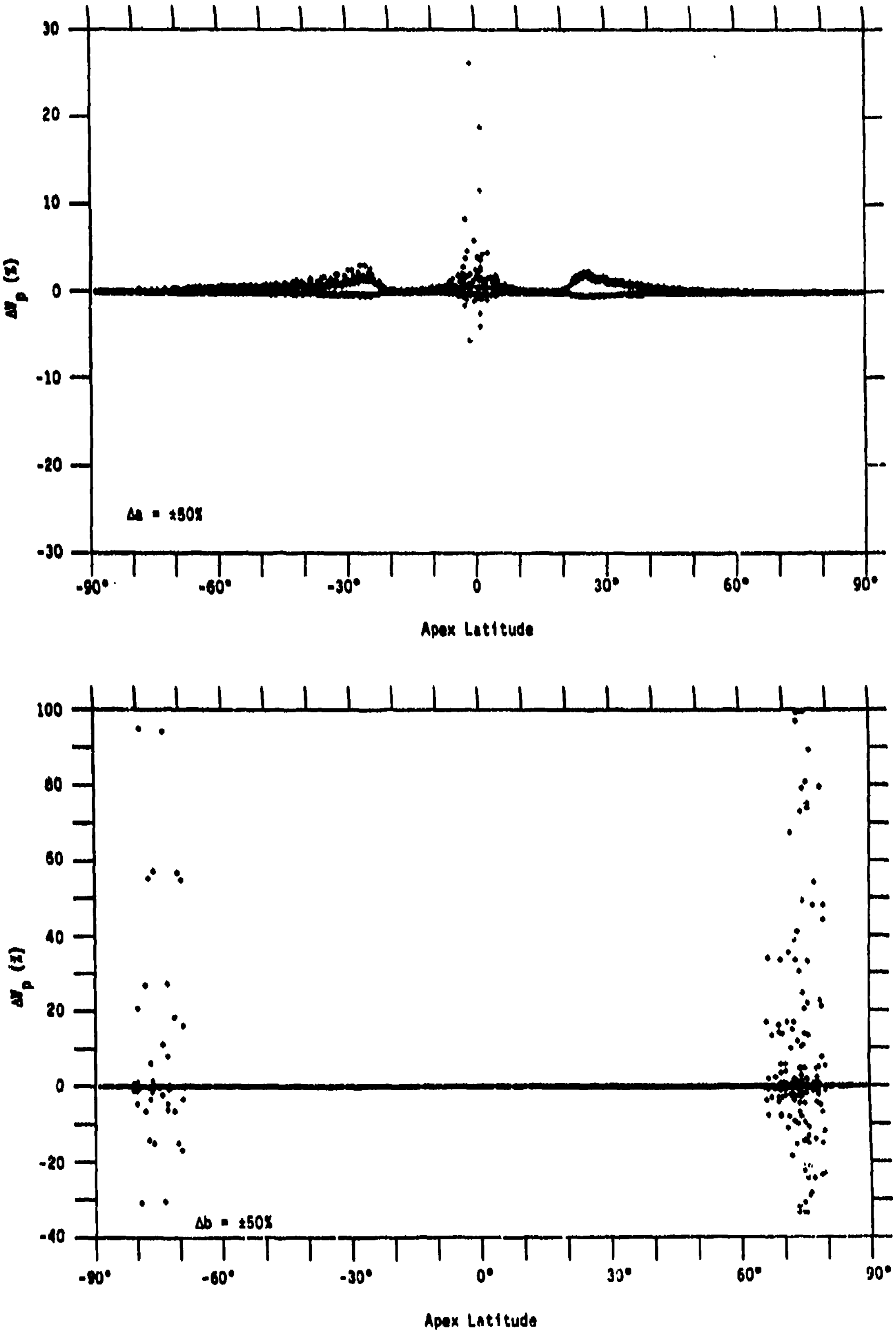

Figure 10. Effects of ±50% errors in axial ratio a (upper plot) and b (lower plot) on parameter V_p.

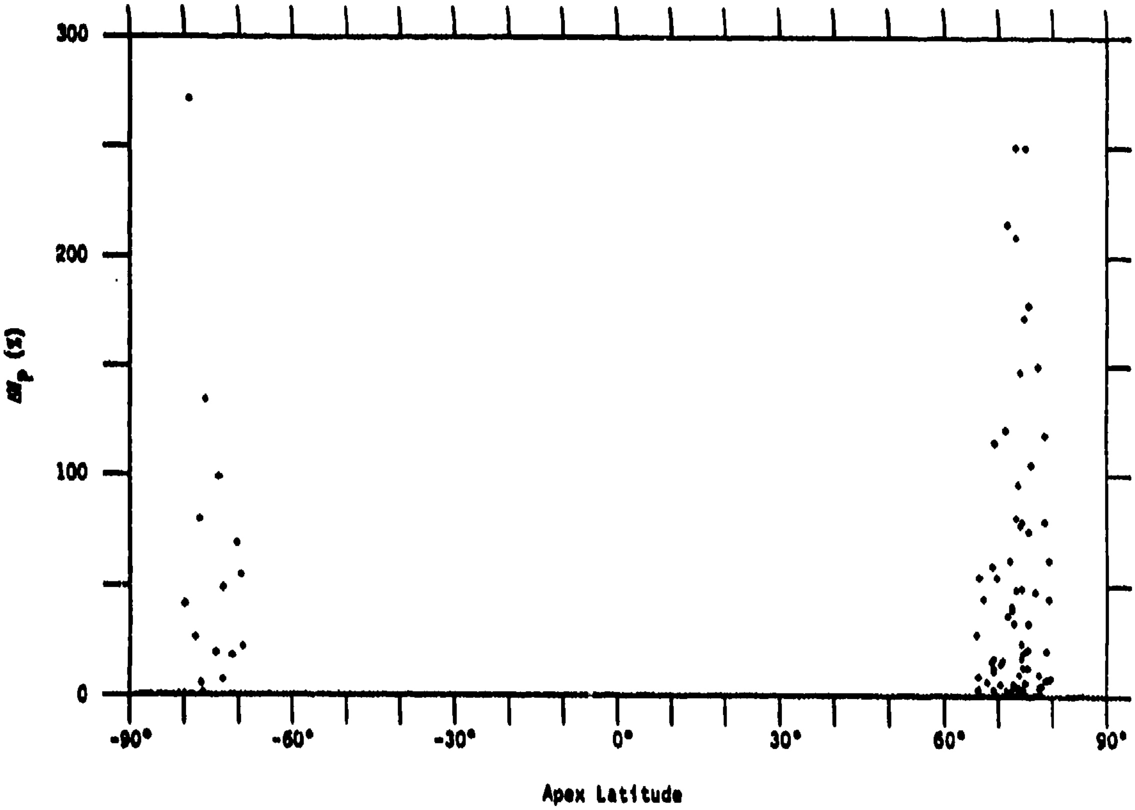

Figure 11. Effect of forcing rod-like irregularities (b=1) at all locations and times on parameter V_p.

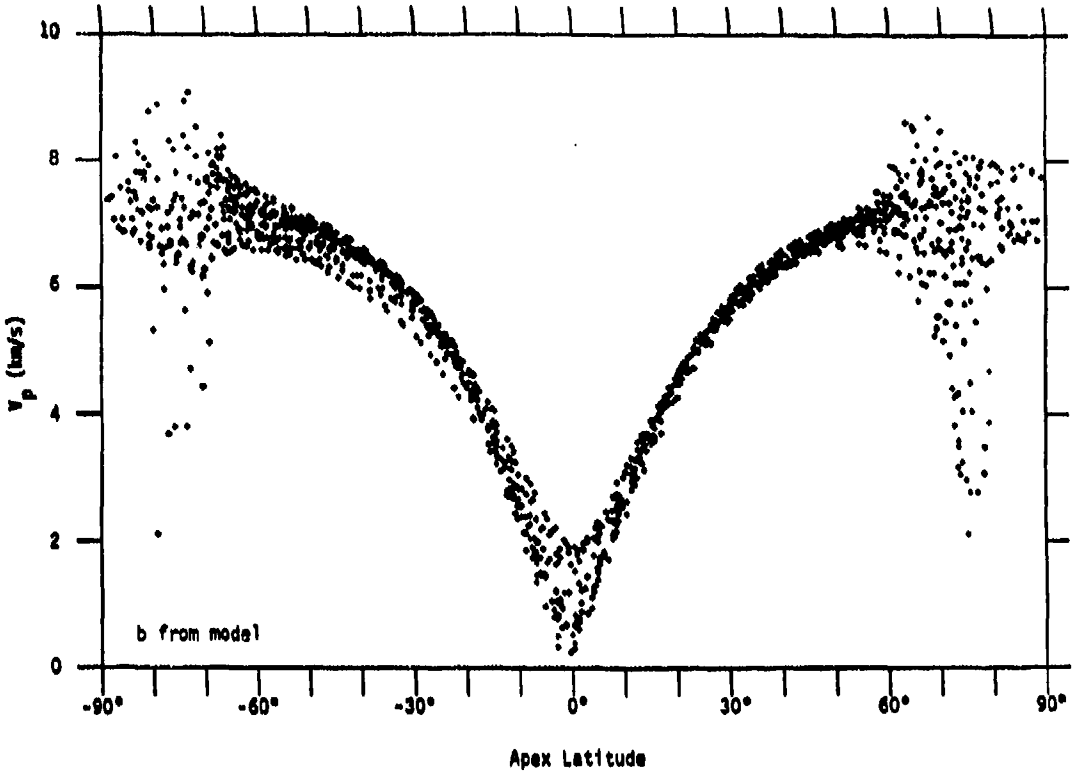

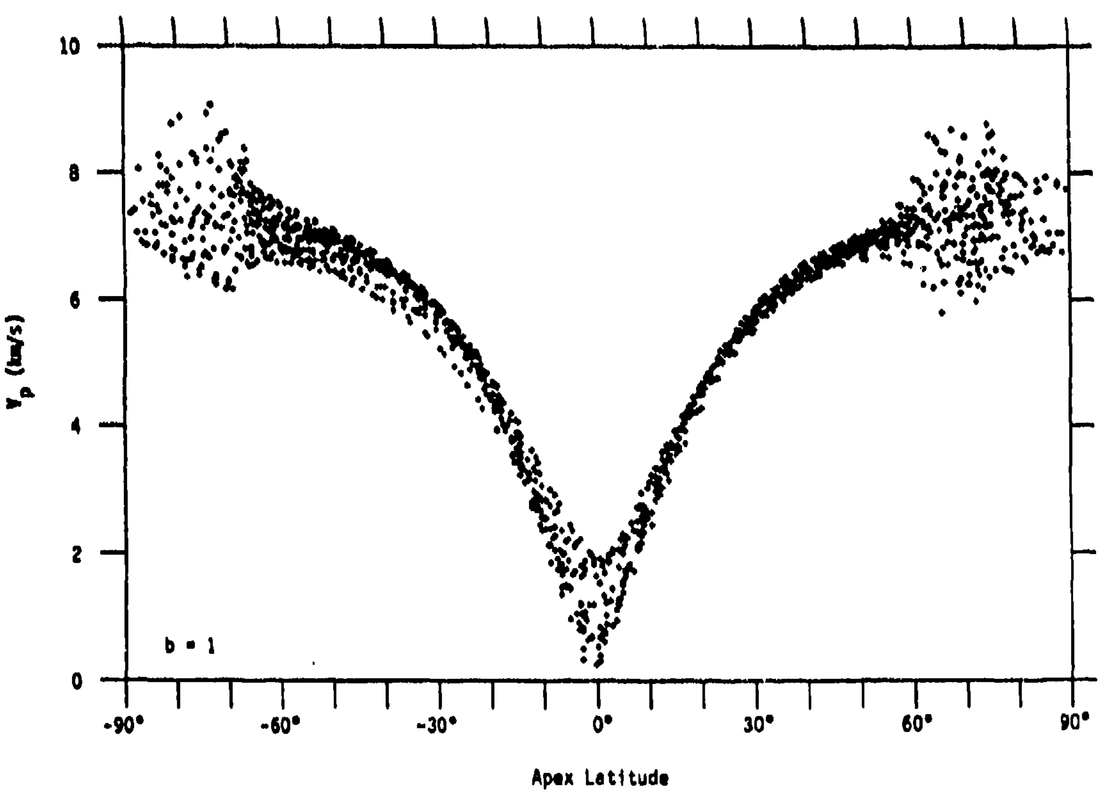

Figure 12. Parameter V_p for 14 dawn-dusk orbits using the model value for b (upper plot) and setting b=1 everywhere (lower plot).

times where the largest errors occur will be limited, but they are in latitude regimes of interest.

A second potential source of error in v_p is errors in the measured, or modeled, values of the *in situ* drift velocity. Figure 13 shows the effect on v_p of removing the drift velocity from the calculation. The errors range from $\pm$~25% at high latitudes to $\pm$~100% at equatorial latitudes. The overall RMS error was 10%, with 16% at equatorial latitudes and 8% at high latitudes. The larger errors at equatorial latitudes are due to the east-west component of the drift velocity, which changes the angle between the vector velocity of the irregularities with respect to the satellite and the local geomagnetic field vector. When this angle is small to begin with, as is the case for DMSP orbits in the equatorial region, v_p is very sensitive to this angle.

The effects of errors in the horizontal drift velocities in the across- (u_h) and along- (u_r) orbit track are shown in Figure 14. The upper plot shows the errors introduced by $\pm$~50% errors in u_r and the lower plot for $\pm$~50% errors in u_h. [Note: Errors in v_p introduced by errors in the vertical component of the drift velocity, u_v, were routinely <1%.] The errors induced in v_p by errors in u_r are small at equatorial and mid latitudes (<1%), and are bounded by $\pm$~15% at high latitudes. The errors induced by errors in u_h are smaller at high latitudes (<10%), but can be much larger in the equatorial region (up to 60%) for the reasons discussed in the previous paragraph. The overall/equatorial/high latitude RMS values for the two cases were 7%/9%/2% for errors in u_h and 2%/<1%/4% for errors in u_r.

Although it is relatively straightforward to estimate the propagation of errors from the axial ratios or the drift velocities to v_p, it is not so simple to make estimates of what errors are to be expected in the parameters themselves. Both axial ratios must be provided from a model (taken from the WBMOD scintillation model and slightly modified) which is based on values inferred from observations of phase scintillation rather than direct observations of these parameters. While it appears errors in axial ratio a will not

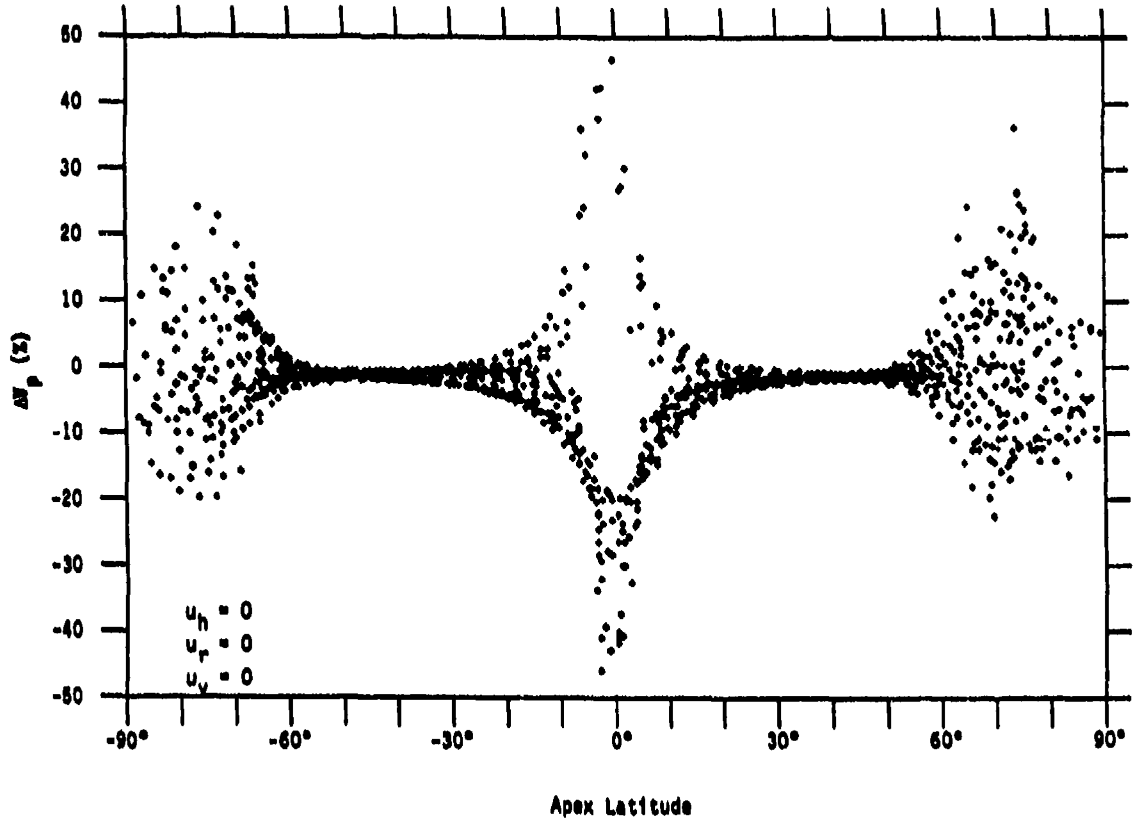

Figure 13. Effect of removing *in-situ* drift velocity on parameter V_p.

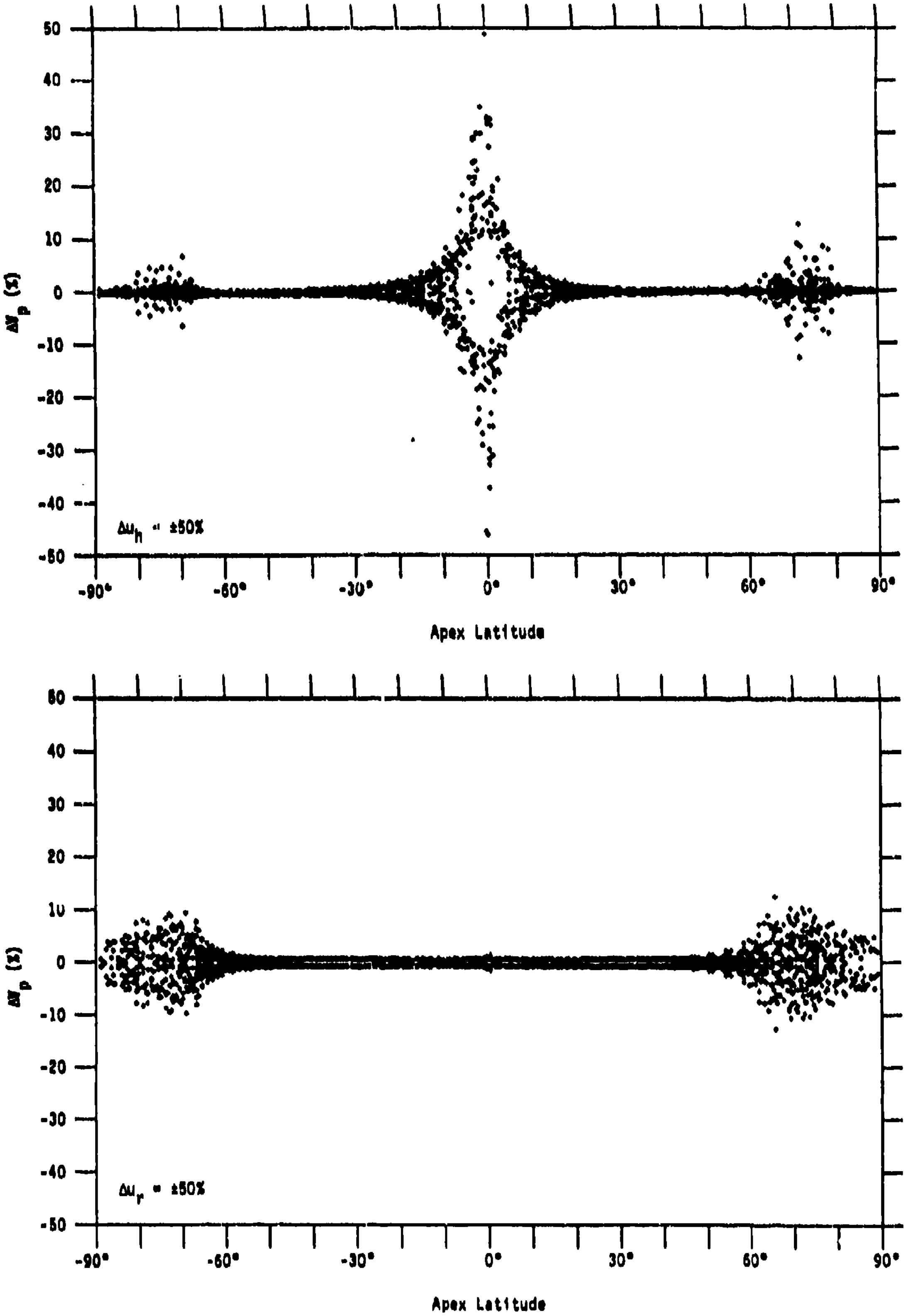

Figure 14. Effect of ±50% errors in the horizontal cross-orbit (upper plot) and along-orbit (lower plot) drift velocities on parameter V_p.

drastically effect v_p, errors in axial ratio b can cause errors in v_p greater than 100%. Unfortunately, there is more confidence in the model for a than for b, and no good estimate of how "bad" the model for b is. The estimate of $\pm$-50% used in the parametric study is probably as good as any at this time.

The outlook is not quite so bleak for estimating errors in the drift velocities, assuming that drift velocity measurements are available from the SSIES Drift Meter (DM) and Retarding Potential Analyzer (RPA) sensors. The DM sensor will provide estimates of u_h and u_v, and the RPA will provide u_r. In parametric studies conducted while developing software to process these data,[7] it was found that the probable minimum RMS error in these measurements was 30 m/s for the DM measurements and 100 m/s for the RPA measurement. Figure 15 shows the percent error in v_p for the dawn-dusk orbits for errors of $\pm$-50 m/s in u_h and u_v and $\pm$-150 m/s in u_r. The $\pm$-2% offsets shown in the figure are due to the errors in u_r, and the scatter at equatorial and high latitudes is due to errors in u_h. The RMS error at all latitudes is 2%, dominated by the error in u_r, and the 99th percentile is about 6%.

If the drift velocities are not available, however, errors on the order of those shown in Figure 13 must be accepted or a model for the drift velocity must be used. While it is unlikely that a simple model will provide accurate drift velocity measurements at high latitudes, it may be possible to model the equatorial east-west drifts to within 50%. Figure 16 shows the expected errors in v_p for the case where no drift velocities are used at high latitudes, and a model with accuracies of $\pm$-50% is used at equatorial latitudes. The RMS errors in v_p for this case are 7% for all latitudes, 9% at equatorial latitudes, and 8% at high latitudes with 99th percentile values of about 25%.

In summary, the expected errors in v_p are as follows:

a. If reasonably good observations of the *in situ* drift velocities are available, errors in v_p will be on the order of a few percent at equatorial and mid latitudes and at high latitudes where

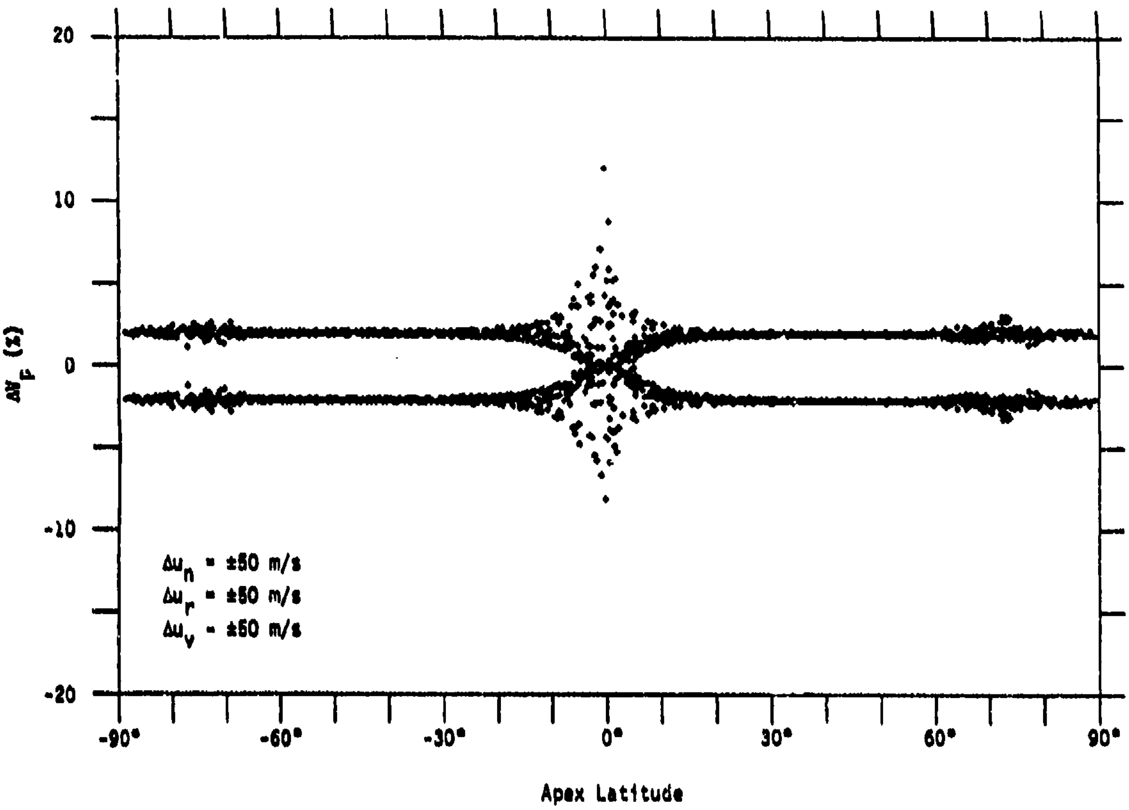

Figure 15. Effect of expected minimum errors in drift velocity measurements on parameter V_p.

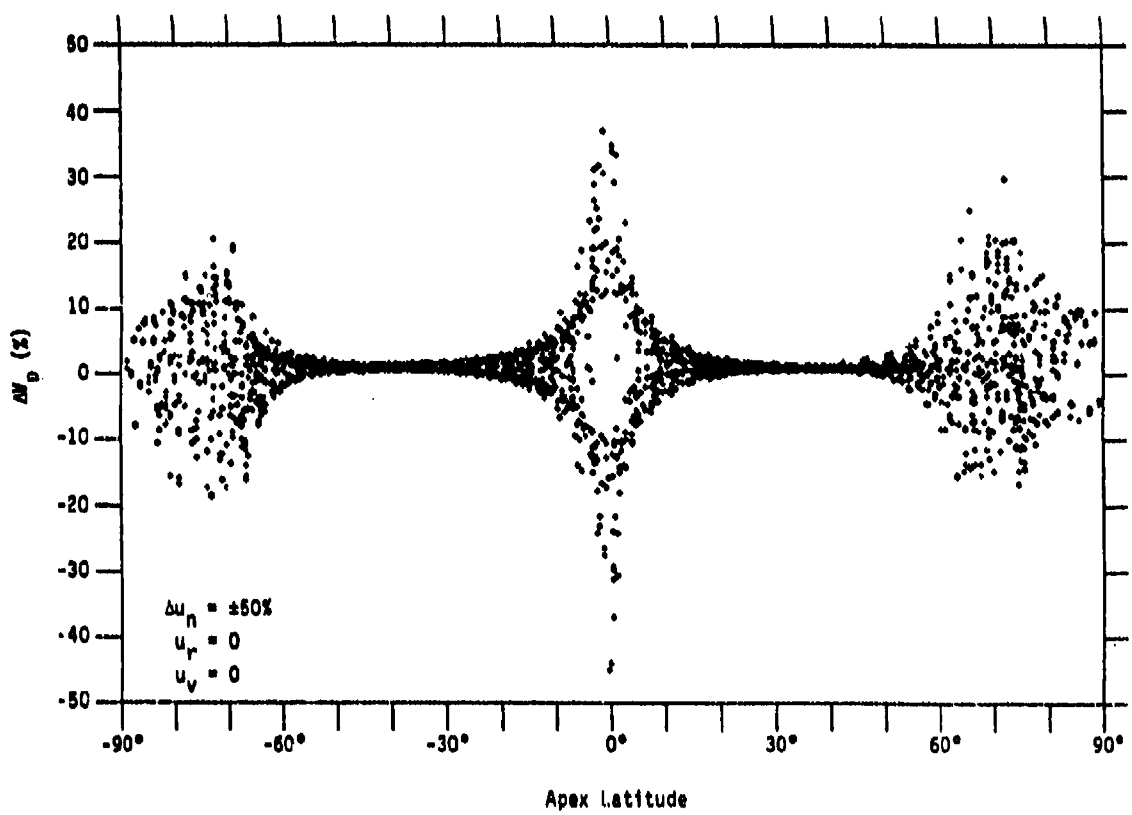

Figure 16. Effect of using a model for u_h with ±50% errors and setting u_r and u_v to zero on parameter V_p.

the irregularities are rod-like. At high latitudes, where they may be sheet-like (most probably in the evening-side of the auroral oval), the RMS errors will be on the order of 15-25%, with errors greater than 100% not uncommon, due strictly to uncertainties in (1) where to switch from rods to sheets and (2) the value to use for axial ratio b for sheet-like irregularities.

b. If observations are not available, the expected RMS errors in both the equatorial region and the high latitude region (away from the region of sheet-like irregularities) increase to about 10% due to uncertainties in the drift velocities. Errors in the high latitude region where sheet-like irregularities may be found will probably increase to 20-30%.

Figure 17 closes the loop on this part of the study, demonstrating the expected RMS error in C_k for a given RMS error in v_p. The RMS ΔC_k values were calculated using the assumed distribution of q used in the previous calculations (a gaussian distribution centered at 1.8, with 1/e-width of 0.6). In the range -20% to +20%, the relationship between the two is nearly linear, so the expected errors in v_p described in the previous paragraph are fairly good estimates for the expected RMS errors in C_k due to errors in v_p.

3.5 Summary of C_k Uncertainties

In the preceding sections we found that the expected errors in C_k due to processing-induced errors in q and T_1 or in q and f_c are on the order of 5-10%, and the errors due to errors/uncertainties in the calculated value of v_p range from a few percent to over 100%. It is not surprising, therefore, to find that the controlling factor on how accurately C_k can be measured is the uncertainties in v_p. This can be seen in Tables 3a and 3b, which summarize the expected uncertainties in C_k as a function of v_p and Δv_p for each of the two methods of calculating C_k. When the uncertainties in v_p are low, i.e. when the axial ratios and *in situ* drift velocities are determined accurately, the uncertainties in C_k will be on the order of 5-15%. This will usually be the case in the equatorial regions. As the uncertainties in v_p increase, however, the uncertainties in C_k will increase roughly

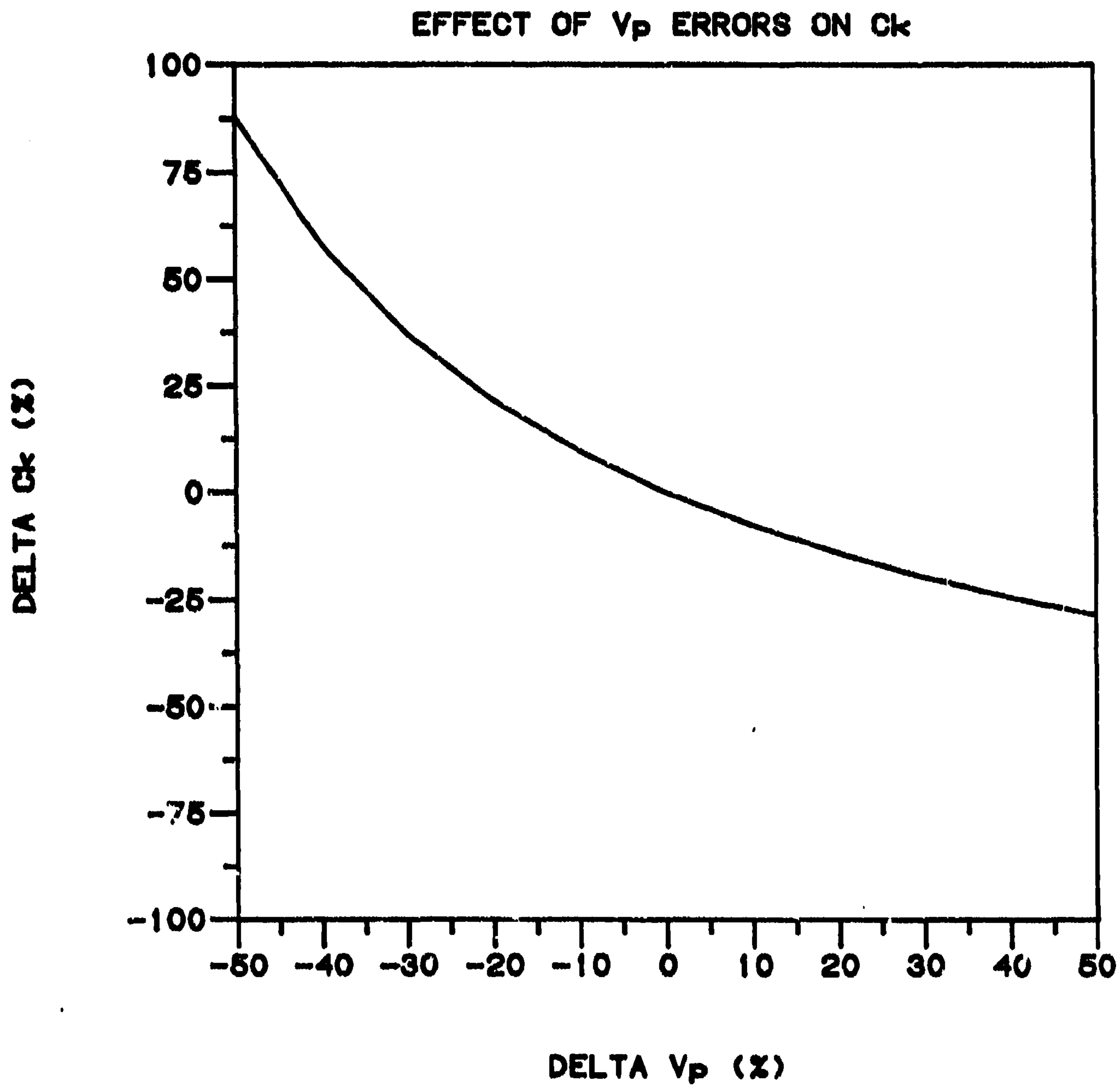

Figure 17. Effect of errors in parameter V_p on C_k.

TABLE 3a. Variation of ΔC_k (%) as a function of v_p and Δv_p for C_k calculated from T_1 and q.

Δv_p	ΔC_k						
	1000.	2000.	3000.	4000.	5000.	6000.	7000.
5.0	7.5	7.0	7.5	8.2	8.8	9.3	9.9
15.0	14.9	14.5	14.8	15.1	15.4	15.8	16.1
25.0	24.8	24.5	24.6	24.8	25.0	25.2	25.5
50.0	66.5	65.9	65.8	65.8	65.9	66.0	66.1

TABLE 3b. Variation of ΔC_k (%) as a function of v_p and Δv_p for C_k calculated from $\langle \Delta N_e^2 \rangle$ and q.

Δv_p	ΔC_k						
	1000.	2000.	3000.	4000.	5000.	6000.	7000.
5.0	7.3	8.9	10.3	11.5	12.4	13.1	13.8
15.0	14.6	15.5	16.4	17.2	17.9	18.5	19.0
25.0	24.4	25.1	25.7	26.3	26.8	27.3	27.7
50.0	65.6	65.9	66.3	66.7	67.1	67.5	67.8

linearly in Δv_p. This will occur in those regions where the shape of the irregularities is in question, i.e. whether they are rod-like or sheet-like, and where the *in situ* drift velocities are not well observed or modeled. These uncertainties will be greatest at high latitudes, particularly (1) during geomagnetic disturbances, when the drift velocities become difficult to measure or model, (2) in and near the evening sector of the auroral oval, where sheet-like irregularities are found, and (3) near the dayside cusp and nightside exit regions of the high-latitude convection pattern and the velocity shear regions near the boundaries of the high-latitude current systems, where the drift velocities can change dramatically both in space and time.

4. PARAMETRIC STUDIES: UNCERTAINTIES IN C_kL

The objective of the second phase of parametric studies was to determine the level of uncertainty in estimates of C_kL made from the estimate of C_k at an altitude of (nominally) 830km. Two studies were planned, one focusing on the effects of uncertainties in the variation of the background ionospheric electron density with height, and the second on the effects of uncertainties in the variation of the irregularity distribution with altitude. The first study was completed during the period covered by this report, the second will be completed during the next contract year.

4.1 Calculation of C_kL From C_k

In order to calculate an estimate of C_kL from an observation of C_k at some altitude, h_s, the following assumptions must be made:

(1) The geometry of the irregularities and the slope of the PDS of the irregularities are relatively constant throughout the irregularity layer.

(2) The variation of C_k, or $\langle \Delta N_e^2 \rangle$, with altitude is known.

(3) The altitude at which the measurement is made is within the irregularity layer.

(4) The measured C_k is representative of conditions throughout the irregularity layer.

(For the time being, we will beg the issue as to whether any of these assumptions are valid or warranted but will accept them as being reasonable.) Assuming that the irregularity PDS and geometry remain fairly constant throughout the irregularity layer, C_k can be related to C_kL through

$$C_kL = \int_{h_b}^{h_t} C_k(h)\, dh \qquad [5]$$

where h_b and h_t are the top and bottom of the irregularity layer. Since C_k is proportional to $\langle \Delta N_e^2 \rangle$, this can be rewritten

$$\frac{C_k L}{C_k(h_s)} = \frac{\int_{h_s}^{h_t} \langle \Delta N_e{}^2 \rangle \, dh}{\langle \Delta N_e{}^2 \rangle_s} \qquad [6]$$

where $C_k(h_s)$ and $\langle \Delta N_e{}^2 \rangle_s$ are measured at the satellite altitude. At this point some model for the height variation of $\langle \Delta N_e{}^2 \rangle$ is required.

The model for $\langle \Delta N_e{}^2 \rangle$ must specify (1) the height range over which irregularities are found (h_b and h_t), and (2) the variation of $\langle \Delta N_e{}^2 \rangle$ over that range. A sample model would be to assume that the irregularity layer extends from h_mF2 to the satellite height, h_s, and that $\langle \Delta N_e{}^2 \rangle^{1/2}/N_e$ remains constant throughout the layer. For this case, Equation [6] becomes

$$C_k L = \frac{\int_{h_mF2}^{h_s} N_e{}^2(h) \, dh}{N_e{}^2(h_s)} \; C_k(h_s) \qquad [7]$$

which depends solely on the topside electron density profile between h_mF2 and the satellite altitude. While this sole dependence on $N_e(h)$ is due to the assumed variation of $\langle \Delta N_e{}^2 \rangle$ with height, it is not unreasonable to assume that the conversion of C_k to $C_k L$ will depend in some way on the topside electron density profile.

An effective irregularity-layer thickness parameter, L_{eff}, can be defined as the ratio of $C_k L$ to $C_k(h_s)$. From Equation [7], valid for the case $\langle \Delta N_e{}^2 \rangle^{1/2}/N_e$ = constant, L_{eff} is then

$$L_{eff} = \frac{\int_{h_mF2}^{h_s} N_e{}^2(h) \, dh}{N_e{}^2(h_s)}. \qquad [8]$$

The calculation of C_kL from C_k is then just

$$C_kL = C_k(h_s)L_{eff}. \qquad [9]$$

For a simple Chapman-layer topside with a constant scale height, the integral in Equation [8] can be evaluated analytically to provide

$$L_{eff} = \gamma H \left[\frac{N_mF2}{N_e(h_s)}\right]^2 \qquad [10]$$

where γ is a function of the height of the satellite above the F2 peak and the scale height given by

$$\gamma = \left[\frac{u_s + 1}{4}\right]\left[e^{-(u_s-2)} - \frac{3}{4}\right]$$

$$u_s = 2 \exp\left\{-\left[\frac{(h_s-h_mF2)}{H}\right]\right\},$$

and N_mF2 is the density at the F2 peak.

The form of Equation [10] suggests the definition of a normalized effective layer-thickness, $\langle L_{eff}\rangle$, in which the ratio of the electron density at the satellite to that at the peak is removed. This parameter would then be defined by

$$\langle L_{eff}\rangle = \left[\frac{N_e(h_s)}{N_mF2}\right]^2 L_{eff}, \qquad [11]$$

and the Equation [9] could be rewritten

$$C_kL = C_k(h_s)\left[\frac{N_e(h_s)}{N_mF2}\right]^2 \langle L_{eff}\rangle. \qquad [12]$$

[Note that for the Chapman profile case, $\langle L_{eff}\rangle$ is just γH.]

4.2 Uncertainties Due to Profile Model

The study of the effects of errors in parameters which define the topside electron density profile will focus on the variation of the two layer-thickness parameters, as defined by Equations [7] (L_{eff}) and [11] ($\langle L_{eff} \rangle$), as functions of f_oF2, h_mF2, Y_t, h_T, and $N_e(h_s)$. The profile model described in the previous section of this report, and the $\langle \Delta N_e^2 \rangle^{1/2}/N_e$ = constant model for the height variation of $\langle \Delta N_e^2 \rangle$, were used for this study.

Rather than look at the variation of errors all along a DMSP orbit, it was decided to focus on those latitudes and local times along the orbits at which measurable levels of scintillation can be expected. Table 4 lists the latitudes and local times selected (basically equatorial at 2200LT, and auroral at all local times), the f_oF2, h_mF2, Y_t, and h_T values used to construct the base profiles, and the values for L_{eff} and $\langle L_{eff} \rangle$ for the base profiles. (Note: Initially a much larger number of profiles were to be processed, but the results were not much different from profile to profile and are well represented by the profiles listed in Table 4.) The variation of L_{eff} and $\langle L_{eff} \rangle$ with each parameter listed above was calculated as follows:

(1) A base profile was constructed using f_oF2, h_mF2, Y_t, and h_T from Table 4. Values for $N_e(h_s)$, L_{eff}, and $\langle L_{eff} \rangle$ were calculated for this profile.

(2) The parameter selected was varied from -20% to +20% of the initial value in 5% steps.

(3) The profile was adjusted to fit the data set consisting of f_oF2, h_mF2, Y_t, h_T, and $N_e(h_s)$ by iteratively changing the α_0 and β profile parameters until $N_e(h_s)$ calculated from the new profile was within 0.1% of the desired value.

(4) Values for L_{eff} and $\langle L_{eff} \rangle$ were calculated for the new profile, and the percent change from the corresponding values for the base profile were calculated.

TABLE 4. Profile parameters for L_{eff} parameteric studies and the values for L_{eff} and $\langle L_{eff} \rangle$ for each basic profile.

Auroral Cases

Case	f_oF2	h_mF2	Y_t	h_T	LT	L_{eff}	$\langle L_{eff} \rangle$
A-01	1.5	225	100	1200	0600	5.44E+4	89.3
A-02	1.5	225	100	1200	1000	2.61E+4	96.7
A-03	1.5	225	100	1200	1800	3.16E+4	91.9
A-04	1.5	225	100	1200	2200	1.11E+5	81.2
A-05	3.0	275	115	1200	0600	2.71E+4	96.4
A-06	3.0	275	115	1200	1000	1.41E+4	106.0
A-07	3.0	275	115	1200	1800	1.63E+4	103.1
A-08	3.0	275	115	1200	2200	4.89E+4	88.4
A-09	6.0	350	150	1200	0600	9.82E+3	115.2
A-10	6.0	350	150	1200	1000	5.93E+3	125.8
A-11	6.0	350	150	1200	1800	6.60E+3	123.9
A-12	6.0	350	150	1200	2200	1.48E+4	107.9
	MHz	km	km	km	HHMM	km	km

Equatorial Cases

Case	f_oF2	h_mF2	Y_t	h_T	LT	L_{eff}	$\langle L_{eff} \rangle$
E-01	5.0	310	120	600	2200	2.72E+4	77.9
E-02	5.0	310	120	800	2200	4.14E+5	76.3
E-03	5.0	310	120	1000	2200	9.80E+5	76.3
E-04	5.0	310	120	1200	2200	1.04E+6	76.3
E-05	10.0	400	150	600	2200	3.78E+3	101.7
E-06	10.0	400	150	800	2200	4.88E+4	91.8
E-07	10.0	400	150	1000	2200	1.15E+5	91.4
E-08	10.0	400	150	1200	2200	1.22E+5	91.4
E-09	15.0	450	235	600	2200	1.25E+3	162.2
E-10	15.0	450	235	800	2200	9.64E+3	134.9
E-11	15.0	450	235	1000	2200	2.20E+4	133.3
E-12	15.0	450	235	1200	2200	2.34E+4	133.3
	MHz	km	km	km	HHMM	km	km

Each of the 24 profile sets listed in Table 4 were processed in this fashion, and statistics for the percent variation in L_{eff} and $\langle L_{eff} \rangle$ were generated for the Auroral and Equatorial cases separately and together. Figure 18 shows samples of the basic profile (solid line) and the $\pm 20\%$ profiles (dotted lines) for all parameters. The profile case used is labeled in each plot.

Summaries of the results are given in Table 5 for the Auroral cases, Table 6 for the Equatorial cases, and Table 7 for all cases combined. The tables list the average, variance, maximum, and minimum values for ΔL_{eff} and $\Delta \langle L_{eff} \rangle$ (%) for the aggregate set under each category. The results for L_{eff} shown in these tables can be summarized as follows:

(1) f_oF2. Uncertainties in this parameter resulted in the largest corresponding uncertainties in L_{eff}, with a range of 55% to +100%. This is unfortunate, as there will probably be no direct observation of this parameter over most of the DMSP orbit.

(2) h_mF2. Although the changes to the profile shape are the most dramatic for this parameter (see Figure 18), the effect of uncertainties in h_mF2 on L_{eff} are much smaller than the effects of uncertainties in either f_oF2 or $N_e(h_s)$. The maximum error in L_{eff} was +17%, obtained from a (probably) pathological case with high h_mF2 and Y_t values and a low h_T value (E-19). With the exception of this one case, the maximum values for ΔL_{eff} were all less than 10%.

(3) h_T. The effect of uncertainties in h_T on L_{eff} was largely a function of whether h_T was below or just above the height of the satellite. The effects were very small for all Auroral cases for which h_T was set to 1200km, and were large only for those Equatorial cases for which h_T was below 1000km. Even for these cases, however, the maximum error in L_{eff} due to uncertainties in h_T was only $\pm 10\%$ for $\pm 20\%$ errors in h_T. On average, the expected errors in L_{eff} due to uncertainty in h_T should not exceed a few percent.

(4) Y_t. This parameter was the only one to show a significant and systematic difference between the Auroral and Equatorial cases. For the Auroral cases, the effects of uncertainties in Y_t were comparable to those due to uncertainties in h_mF2 with a range of -6%

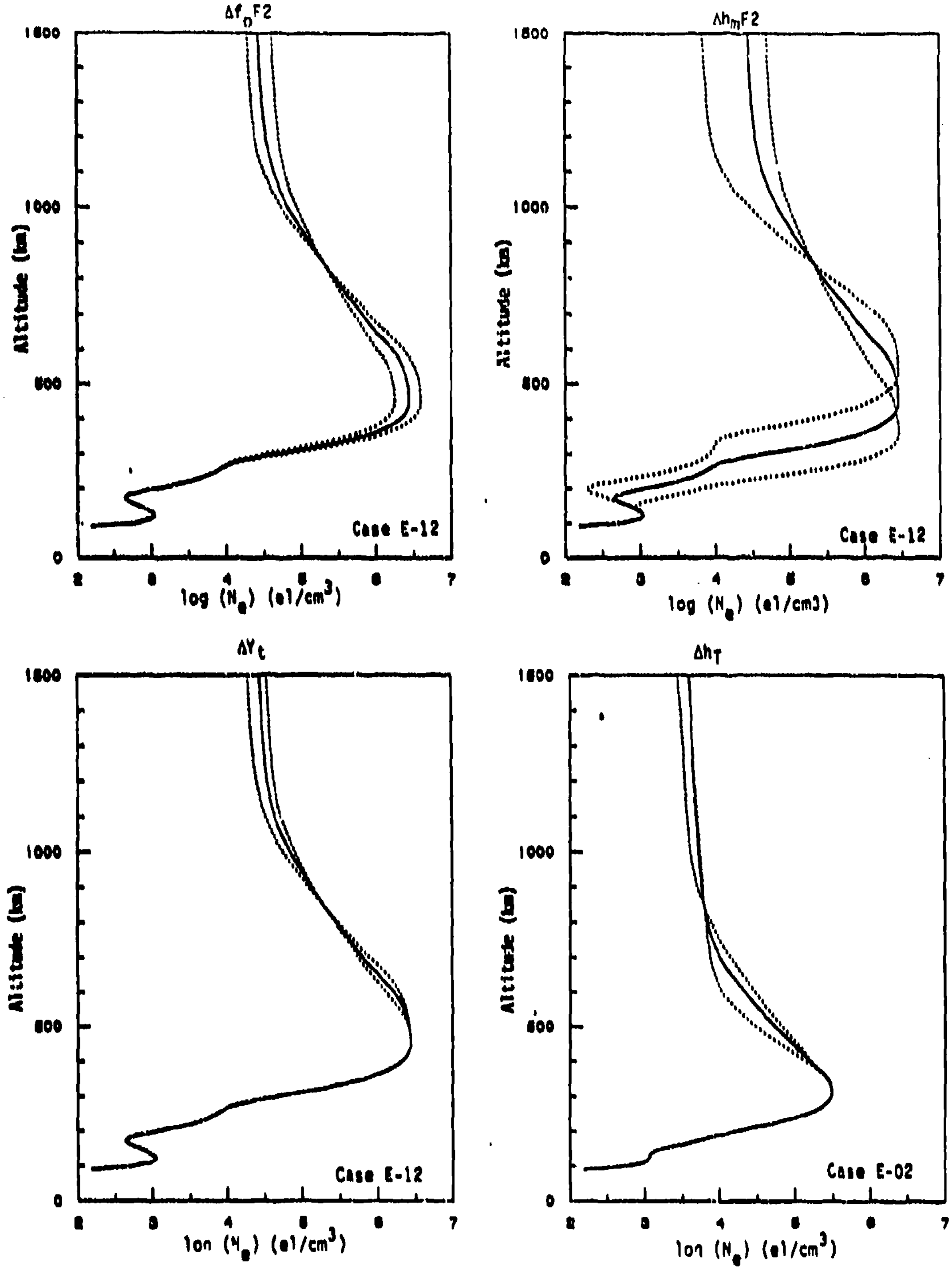

Figure 18. Sample basic profiles (solid curve) and ±20% profiles (dotted curves).

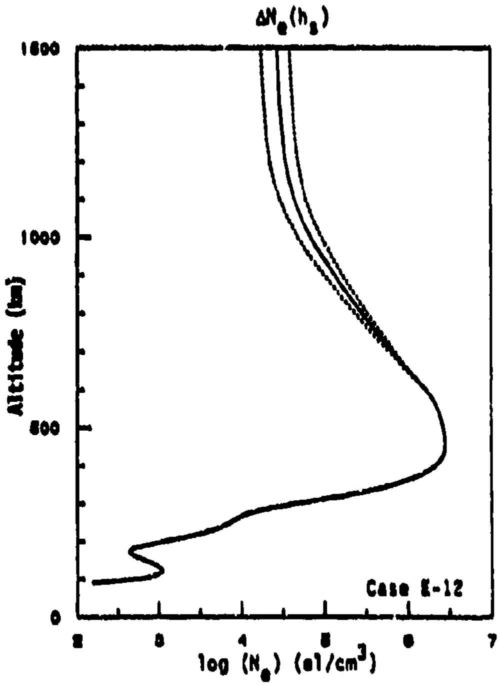

Figure 18. (Continued).

TABLE 5a. Summary of results for parameter L_{eff} (Auroral).

Average ΔL_{eff} (%)

PARAMETER	-20%	-15%	-10%	-5%	+5%	+10%	+15%	+20%
f_oF2	-52.4	-42.0	-30.0	-16.0	18.3	39.0	62.6	89.1
h_mF2	6.9	5.2	3.4	1.7	-1.7	-3.3	-4.8	-6.2
h_T	-2.5	-1.6	-0.9	-0.4	0.3	0.5	0.7	0.8
Y_t	-6.3	-4.9	-3.3	-1.7	1.7	3.4	5.4	7.3
$N_e(h_s)$	47.1	32.4	19.9	9.2	-8.1	-15.0	-21.1	-26.6

RMS ΔL_{eff} (%)

PARAMETER	-20%	-15%	-10%	-5%	+5%	+10%	+15%	+20%
f_oF2	1.4	1.2	0.9	0.5	0.6	1.3	2.2	3.2
h_mF2	1.9	1.3	0.7	0.3	0.3	0.6	0.9	1.2
h_T	0.3	0.2	0.1	0.1	0.1	0.1	0.1	0.2
Y_t	1.2	0.9	0.6	0.3	0.3	0.7	0.9	1.3
$N_e(h_s)$	1.6	1.1	0.6	0.3	0.2	0.5	0.6	0.8

Minimum ΔL_{eff} (%)

PARAMETER	-20%	-15%	-10%	-5%	+5%	+10%	+15%	+20%
f_oF2	-50.1	-40.2	-28.7	-15.3	17.5	37.3	59.8	85.0
h_mF2	2.4	2.2	1.6	0.9	-1.0	-2.1	-3.2	-4.1
h_T	-1.9	-1.2	-0.7	-0.3	0.2	0.3	0.4	0.5
Y_t	-4.7	-3.6	-2.4	-1.2	1.3	2.5	4.0	5.5
$N_e(h_s)$	45.0	30.9	19.0	8	-7.8	-14.3	-20.2	-25.4

Maximum ΔL_{eff} (%)

PARAMETER	-20%	-15%	-10%	-5%	+5%	+10%	+15%	+20%
f_oF2	-54.5	-43.8	-31.4	-16.8	19.2	40.9	65.8	93.7
h_mF2	9.9	7.2	4.6	2.3	-2.2	-4.4	-6.4	-8.5
h_T	-3.0	-1.9	-1.1	-0.5	0.4	0.7	0.9	1.0
Y_t	-9.0	-6.8	-4.8	-2.4	2.3	4.9	7.5	10.1
$N_e(h_s)$	49.4	34.0	20.8	9.6	-8.4	-15.7	-22.1	-27.8

TABLE 5b. Summary of results for parameter $\langle L_{eff} \rangle$ (Auroral).

Average $\Delta\langle L_{eff}\rangle$ (%)

PARAMETER	-20%	-15%	-10%	-5%	+5%	+10%	+15%	+20%
f_oF2	16.4	11.1	6.8	3.1	-2.7	-5.0	-7.0	-8.8
h_mF2	7.0	5.2	3.5	1.7	-1.6	-3.2	-4.7	-6.2
h_T	-2.5	-1.6	-0.9	-0.4	0.3	0.5	0.7	0.8
Y_t	-6.3	-4.8	-3.3	-1.7	1.7	3.5	5.4	7.3
$N_e(h_s)$	-5.7	-4.3	-2.9	-1.4	1.5	2.9	4.3	5.8

RMS $\Delta\langle L_{eff}\rangle$ (%)

PARAMETER	-20%	-15%	-10%	-5%	+5%	+10%	+15%	+20%
f_oF2	3.4	2.2	1.3	0.6	0.5	0.9	1.2	1.5
h_mF2	1.9	1.2	0.7	0.3	0.3	0.6	0.9	1.2
h_T	0.3	0.2	0.1	0.1	0.1	0.1	0.1	0.2
Y_t	1.2	0.9	0.6	0.3	0.3	0.6	0.9	1.3
$N_e(h_s)$	1.0	0.8	0.5	0.3	0.3	0.5	0.8	1.1

Minimum $\Delta\langle L_{eff}\rangle$ (%)

PARAMETER	-20%	-15%	-10%	-5%	+5%	+10%	+15%	+20%
f_oF2	11.1	7.6	4.7	2.2	-1.9	-3.6	-5.2	-6.6
h_mF2	2.4	2.2	1.7	0.9	-1.0	-2.0	-3.0	-4.1
h_T	-1.9	-1.2	-0.7	-0.3	0.2	0.4	0.5	0.5
Y_t	-4.7	-3.6	-2.5	-1.3	1.3	2.7	4.0	5.5
$N_e(h_s)$	-4.2	-3.1	-2.1	-1.0	1.0	2.0	3.0	4.0

Maximum $\Delta\langle L_{eff}\rangle$ (%)

PARAMETER	-20%	-15%	-10%	-5%	+5%	+10%	+15%	+20%
f_oF2	21.8	14.6	8.8	4.0	-3.3	-6.2	-8.6	-10.8
h_mF2	9.9	7.2	4.7	2.3	-2.2	-4.3	-6.4	-8.5
h_T	-3.0	-1.9	-1.1	-0.5	0.4	0.6	0.9	1.0
Y_t	-9.0	-6.8	-4.6	-2.4	2.4	4.9	7.5	10.1
$N_e(h_s)$	-7.1	-5.4	-3.6	-1.8	1.9	3.7	5.6	7.5

TABLE 6a. Summary of results for parameter L_{eff} (Equatorial).

Average ΔL_{eff} (%)

PARAMETER	-20%	-15%	-10%	-5%	+5%	+10%	+15%	+20%
f_oF2	-56.4	-44.8	-32.2	-17.3	20.0	42.8	69.2	99.0
h_mF2	7.2	5.1	3.3	1.6	-1.7	-3.0	-4.1	-5.3
h_T	-3.9	-3.2	-1.8	-1.0	0.8	1.7	2.4	3.0
Y_t	-12.4	-9.4	-6.4	-3.2	3.3	6.6	10.0	13.5
$N_e(h_s)$	51.9	35.5	21.7	10.0	-8.7	-16.2	-22.8	-28.6

RMS ΔL_{eff} (%)

PARAMETER	-20%	-15%	-10%	-5%	+5%	+10%	+15%	+20%
f_oF2	2.2	3.0	2.2	1.2	1.4	2.8	4.6	6.5
h_mF2	4.0	2.6	1.7	0.9	0.7	1.3	1.6	1.9
h_T	3.7	2.7	2.0	1.0	0.9	2.0	2.9	3.8
Y_t	2.0	1.5	1.0	0.5	0.5	1.0	1.4	1.9
$N_e(h_s)$	3.5	2.4	1.5	0.7	0.6	1.1	1.6	2.0

Minimum ΔL_{eff} (%)

PARAMETER	-20%	-15%	-10%	-5%	+5%	+10%	+15%	+20%
f_oF2	-50.0	-36.5	-26.2	-14.2	16.3	35.3	57.1	82.4
h_mF2	4.6	3.1	2.1	0.9	-1.1	-1.9	-2.8	-3.8
h_T	-0.3	-0.2	-5.7	0.0	0.0	0.0	0.0	0.0
Y_t	-8.1	-6.3	-4.2	-2.2	2.2	4.5	6.9	9.5
$N_e(h_s)$	42.8	29.2	17.7	8.2	-7.1	-13.3	-18.5	-23.3

Maximum ΔL_{eff} (%)

PARAMETER	-20%	-15%	-10%	-5%	+5%	+10%	+15%	+20%
f_oF2	-57.6	-46.5	-33.5	-18.0	20.8	44.7	72.3	103.5
h_mF2	17.7	11.6	7.5	3.7	-3.4	-5.9	-8.5	-10.5
h_T	-10.6	-8.4	0.6	-3.0	2.7	5.7	8.4	10.9
Y_t	-15.1	-11.5	-7.7	-3.9	3.9	7.9	11.9	16.1
$N_e(h_s)$	54.1	37.0	22.7	10.5	-9.2	-16.8	-23.7	-29.7

TABLE 6b. Summary of results for parameter $\langle L_{eff} \rangle$ (Equatorial).

Average $\Delta\langle L_{eff} \rangle$ (%)

PARAMETER	-20%	-15%	-10%	-5%	+5%	+10%	+15%	+20%
f_oF2	6.5	5.8	3.5	1.6	-1.3	-2.3	-3.2	-4.0
h_mF2	7.2	5.2	3.4	1.7	-1.6	-3.0	-4.0	-5.2
h_T	-3.9	-3.1	-1.8	-0.9	0.9	1.7	2.4	3.1
Y_t	-12.3	-9.4	-6.3	-3.2	3.3	6.6	10.1	13.5
$N_e(h_s)$	-2.7	-2.0	-1.4	-0.7	0.7	1.4	2.2	2.9

RMS $\Delta\langle L_{eff} \rangle$ (%)

PARAMETER	-20%	-15%	-10%	-5%	+5%	+10%	+15%	+20%
f_oF2	5.3	5.8	3.3	1.5	1.1	2.0	2.6	3.1
h_mF2	4.0	2.6	1.7	0.8	0.8	1.4	1.5	1.9
h_T	3.7	2.8	2.0	1.0	1.0	2.0	2.9	3.9
Y_t	2.0	1.5	1.0	0.5	0.5	1.0	1.5	1.9
$N_e(h_s)$	2.2	1.7	1.2	0.6	0.7	1.3	2.1	2.8

Minimum $\Delta\langle L_{eff} \rangle$ (%)

PARAMETER	-20%	-15%	-10%	-5%	+5%	+10%	+15%	+20%
f_oF2	3.7	2.5	1.5	0.7	-0.6	-1.1	-1.5	-1.9
h_mF2	4.6	3.3	2.1	1.0	-0.9	-1.9	-2.7	-3.6
h_T	-0.3	-0.1	-5.7	0.0	0.0	0.0	0.0	0.0
Y_t	-8.1	-6.2	-4.2	-2.1	2.2	4.5	6.9	9.5
$N_e(h_s)$	-1.2	-0.9	-0.6	-0.3	0.3	0.6	1.0	1.3

Maximum $\Delta\langle L_{eff} \rangle$ (%)

PARAMETER	-20%	-15%	-10%	-5%	+5%	+10%	+15%	+20%
f_oF2	22.3	21.8	12.6	5.5	-4.2	-7.6	-10.1	-12.1
h_mF2	17.8	11.6	7.7	3.7	-3.4	-5.9	-8.3	-10.5
h_T	-10.6	-8.3	0.6	-2.9	2.9	5.7	8.4	11.0
Y_t	-15.1	-11.4	-7.7	-3.9	3.9	8.0	12.0	16.1
$N_e(h_s)$	-8.6	-6.6	-4.5	-2.3	2.5	5.1	7.7	10.5

TABLE 7a. Summary of results for parameter L_{eff} (All cases).

Average ΔL_{eff} (%)

PARAMETER	-20%	-15%	-10%	-5%	+5%	+10%	+15%	+20%
f_oF2	-54.3	-43.4	-31.1	-16.7	19.1	40.9	65.9	94.1
h_mF2	7.0	5.2	3.4	1.6	-1.7	-3.2	-4.5	-5.8
h_T	-3.1	-2.3	-1.4	-0.7	0.6	1.1	1.5	1.9
Y_t	-9.3	-7.1	-4.8	-2.4	2.5	5.0	7.7	10.4
$N_e(h_s)$	49.5	33.9	20.8	9.6	-8.4	-15.6	-22.0	-27.6

RMS ΔL_{eff} (%)

PARAMETER	-20%	-15%	-10%	-5%	+5%	+10%	+15%	+20%
f_oF2	2.7	2.7	2.0	1.1	1.3	2.9	4.9	7.1
h_mF2	3.1	2.1	1.3	0.7	0.6	1.1	1.3	1.7
h_T	2.5	2.1	1.5	0.8	0.7	1.5	2.2	2.9
Y_t	3.4	2.6	1.7	0.9	0.9	1.8	2.6	3.5
$N_e(h_s)$	3.6	2.4	1.5	0.7	0.6	1.0	1.4	1.8

Minimum ΔL_{eff} (%)

PARAMETER	-20%	-15%	-10%	-5%	+5%	+10%	+15%	+20%
f_oF2	-50.0	-36.5	-26.2	-14.2	16.3	35.3	57.1	82.4
h_mF2	2.4	2.2	1.6	0.9	-1.0	-1.9	-2.8	-3.8
h_T	-0.3	-0.2	-5.7	0.0	0.0	0.0	0.0	0.0
Y_t	-4.7	-3.6	-2.4	-1.2	1.3	2.5	4.0	5.5
$N_e(h_s)$	42.8	29.2	17.7	8.2	-7.1	-13.3	-18.5	-23.3

Maximum ΔL_{eff} (%)

PARAMETER	-20%	-15%	-10%	-5%	+5%	+10%	+15%	+20%
f_oF2	-57.6	-46.5	-33.5	-18.0	20.8	44.7	72.3	103.5
h_mF2	17.7	11.6	7.5	3.7	-3.4	-5.9	-8.5	-10.5
h_T	-10.6	-8.4	0.6	-3.0	2.7	5.7	8.4	10.9
Y_t	-15.1	-11.5	-7.7	-3.9	3.9	7.9	11.9	16.1
$N_e(h_s)$	54.1	37.0	22.7	10.5	-9.2	-16.8	-23.7	-29.7

TABLE 7b. Summary of results for parameter $\langle L_{eff} \rangle$ (All cases).

Average $\Delta\langle L_{eff} \rangle$ (%)

PARAMETER	-20%	-15%	-10%	-5%	+5%	+10%	+15%	+20%
f_oF2	11.6	8.5	5.1	2.3	-2.0	-3.7	-5.1	-6.4
h_mF2	7.1	5.2	3.4	1.7	-1.6	-3.1	-4.4	-5.7
h_T	-3.1	-2.3	-1.3	-0.7	0.6	1.1	1.5	1.9
Y_T	-9.3	-7.1	-4.8	-2.4	2.5	5.1	7.7	10.4
$N_e(h_s)$	-4.2	-3.2	-2.1	-1.1	1.1	2.2	3.2	4.4

RMS $\Delta\langle L_{eff} \rangle$ (%)

PARAMETER	-20%	-15%	-10%	-5%	+5%	+10%	+15%	+20%
f_oF2	6.6	5.1	3.0	1.4	1.1	2.0	2.8	3.4
h_mF2	3.1	2.1	1.3	0.6	0.6	1.1	1.3	1.7
h_T	2.5	2.0	1.5	0.8	0.8	1.5	2.2	3.0
Y_t	3.4	2.6	1.7	0.9	0.9	1.8	2.6	3.5
$N_e(h_s)$	2.3	1.8	1.2	0.6	0.6	1.3	1.9	2.6

Minimum $\Delta\langle L_{eff} \rangle$ (%)

PARAMETER	-20%	-15%	-10%	-5%	+5%	+10%	+15%	+20%
f_oF2	3.7	2.5	1.5	0.7	-0.6	-1.1	-1.5	-1.9
h_mF2	2.4	2.2	1.7	0.9	-0.9	-1.9	-2.7	-3.6
h_T	-0.3	-0.1	-5.7	0.0	0.0	0.0	0.0	0.0
Y_t	-4.7	-3.6	-2.5	-1.3	1.3	2.7	4.0	5.5
$N_e(h_s)$	-1.2	-0.9	-0.6	-0.3	0.3	0.6	1.0	1.3

Maximum $\Delta\langle L_{eff} \rangle$ (%)

PARAMETER	-20%	-15%	-10%	-5%	+5%	+10%	+15%	+20%
f_oF2	22.3	21.8	12.6	5.5	-4.2	-7.6	-10.1	-12.1
h_mF2	17.8	11.6	7.7	3.7	-3.4	-5.9	-8.3	-10.5
h_T	-10.6	-8.3	0.6	-2.9	2.9	5.7	8.4	11.0
Y_t	-15.1	-11.4	-7.7	-3.9	3.9	8.0	12.0	16.1
$N_e(h_s)$	-8.6	-6.6	-4.5	-2.3	2.5	5.1	7.7	10.5

to +7%. For the Equatorial cases, however, the ΔL_{eff} values were twice that of the Auroral cases, with a range of -12% to +14%.

(5) $N_e(h_s)$. The effects of uncertainties in this parameter on L_{eff} were second only to the effects of uncertainties in f_oF2, ranging from roughly +50% to -30%. Fortunately, this parameter will be measured directly at the satellite with a probable error of ±5% or so, which translates to an uncertainty in L_{eff} of roughly ±10%.

The results for $\Delta\langle L_{eff}\rangle$ were similar, with the notable exception of the level of effects due to uncertainties in the two density parameters, f_oF2 and $N_e(h_s)$. With the removal of the density ratio from L_{eff}, the effects of ±20% errors in these two parameters drop to ranges of +12% to -6% and -4% to +4% for f_oF2 and $N_e(h_s)$, respectively. The results for the other parameters were identical to those for L_{eff} since both f_oF2 and $N_e(h_s)$ were held constant (or nearly so) for these cases.

The main difficulty in using these results is assessing what level of errors to expect in each of the parameters and how they may be correlated with one another. For example, errors in either f_oF2 or $N_e(h_s)$ result in large errors in both L_{eff} and C_kL. However, if the errors in these parameters are strongly correlated such that the ratio between $N_e(h_s)$ and N_mF2 is nearly constant, the errors in C_kL will be, at most, more on the level of those found in $\langle L_{eff}\rangle$. This was actually done for case E-07, i.e. f_oF2 was stepped from -20% to +20% and $N_e(h_s)$ was changed to keep the density ratio constant, and the error in L_{eff} was zero. We can, however, at least make the following observations:

(1) The most crucial profile parameters for making accurate estimates of C_kL, assuming that the variation of $\langle\Delta N_e^2\rangle$ with height is described by $\langle\Delta N_e^2\rangle^{1/2}/N_e$ = constant, are the electron density at the profile peak and at the satellite. Errors of ±20% in these can lead to errors in C_kL of a factor of 2.

(2) Errors in h_T will have no appreciable effect on C_kL unless the transition height occurs near or below the satellite altitude. This should only be a problem during night in the equatorial region

during periods of low sunspot number, and the effect on C_kL should not exceed roughly 10%.

(3) The effect of errors in the height and shape of the peak (h_mF2 and Y_t) on C_kL will typically not exceed 5-8%.

(4) Noting that (a) the range of $\langle L_{eff} \rangle$ is also much less than that of L_{eff}, and (b) the lesser effect of errors in the two density parameters on $\langle L_{eff} \rangle$, it may make sense to develop a global model for $\langle L_{eff} \rangle$ and couple it with observations of $N_e(h_s)$ and values for f_oF2 from a good model or analysis to calculate C_kL rather than attempting to model or calculate L_{eff} directly.

In closing, it should be remembered that these results pertain only to the case where (1) the satellite is within the irregularity layer and has taken a sample representative of the entire layer, (2) the height distribution of the irregularities can be modeled by $\langle \Delta N_e^2 \rangle^{1/2}/N_e$ = constant in a layer between h_mF2 and h_s, and (3) the height variation of the electron density profile in the topside can be approximated by a two-component plasma (O+ and H+) in diffusive equilibrium.

5. CONCLUSION

This report presented the results of studies conducted during the first year of this project aimed at developing methods for calculating estimates of the ionospheric irregularity parameter C_kL from *in situ* observations of the ionosphere from the DMSP SSIES sensor package. It was found that the two methods for calculating C_k from the ion density data had the same levels of uncertainty in the final value for C_k as long as the data were properly processed. The processing methods found to provide the best estimates for C_k were as follows:

(1) T_1/q method. Detrend the data set using (at least) a quadratic detrender; window the data with a 30% split-bell cosine taper; calculate and estimate the PDS using an FFT of the windowed data; smooth the PDS using a 5-point, centered, binomial-weight smoother; calculate estimates of T_1 and q from a log-linear least-squares fit to the smoothed PDS over the frequency range 0.5-7.0 Hz.

(2) $\langle \Delta N_e^2 \rangle/q$ method. Detrend the data using a Fourier-type detrender; calculate $\langle \Delta N_e^2 \rangle$ from the detrended data set; calculate an estimate for q using the detrended data and the procedures described above for the T_1/q method.

The critical element for the T_1/q method is that the data need to be windowed prior to the FFT and the resulting PDS smoothed prior to the log-linear fit to obtain the best estimates for T_1 and q. For the $\langle \Delta N_e^2 \rangle/q$ method, the critical elements are to (1) use a frequency-domain filter for detrending so that the cutoff frequency is well defined, and (2) use an observed value for q rather than a mean, or modeled, value. Using these processing methods, the resulting uncertainties in C_k due to uncertainties in parameters obtained from the density data set are on the order of 5 to 10%.

The effects of uncertainties in the calculated value of the effective probe velocity, v_p, on C_k were also investigated, and were found to produce uncertainties in C_k in a range from a few percent to over 100%. The main sources of uncertainty in v_p are the shape of the irregularities (rod-like or sheet-like) and the *in situ* drift velocity of the irregularities.

The total level of uncertainties in C_k from all sources was found to be as follows:

(1) Equatorial. Uncertainties should be on the order of 5 to 10% when the *in situ* drift velocities are known, and 10-20% when they are not.

(2) Auroral/polar. Uncertainties should be on the order of 5 to 10% when the *in situ* drift velocities and the irregularity shape are well known, 15 to 30% when the drift velocities are not well known, and 25 to >100% when neither are well known.

In both regimes, the uncertainty in C_k will increase roughly linearly with increasing uncertainty in v_p. The largest source of uncertainty is the shape of the irregularities at auroral/polar latitudes. Since this cannot be directly measured from the SSIES data set, a good model must be provided for the two axial ratio parameters, a and b.

A method was developed for calculating an estimate for C_kL from C_k at the satellite altitude. Two "layer thickness" parameters were defined, an effective layer thickness, L_{eff}, defined such that

$$C_kL = C_k x L_{eff}$$

and a normalized effective layer thickness, $\langle L_{eff} \rangle$, defined by

$$\langle L_{eff} \rangle = [N_e(h_s)/N_mF2] x L_{eff}.$$

Both are functions of the altitude range of the irregularity layer and the altitude variation of $\langle \Delta N_e^2 \rangle$ within the layer. A parametric study or uncertainties in L_{eff} and $\langle L_{eff} \rangle$ was conducted in which the irregularity layer was assumed to extend from the F2-layer peak to the altitude of the satellite, $\langle \Delta N_e^2 \rangle^{1/2}/N_e$ was assumed to be constant with altitude throughout the layer, and the background ionospheric electron density was modeled by an adjustable diffusive-equilibrium distribution.

The major results of this study were:

(1) The most crucial profile parameters for making accurate estimates of C_kL are the electron density at the F2-layer peak and at the satellite altitude. Errors of only 20% in f_oF2 can result in 100% errors in C_kL.

(2) The effects of errors in the densities are much less on $\langle L_{eff} \rangle$ due to the decoupling of the densities from this parameter.

(3) The effects of $\pm$20% errors in all other profile parameters resulted in less than 10% errors in C_kL.

Based on this study, future development of techniques for converting C_k to C_kL will focus on developing a global model for $\langle L_{eff} \rangle$ which can be coupled to an external source for the densities to calculate L_{eff}. This investigation of the uncertainties in the conversion of C_k to C_kL will be continued in the next year with a study of the effects of uncertainties in the height distribution of the irregularities.

REFERENCES

[1] Fremouw, E.J. and Lansinger, J.M., A Computer Model for High-Latitude Phase Scintillation Based on WIDEBAND Satellite data From Poker Flat, DNA Report 5685F, Defense Nuclear Agency, Washington, DC, February 1981.

[2] Rino, C.L., "A Power Law Phase Screen Model for Ionospheric Scintillation, 1. Weak Scatter," Radio Sci., 14, pp 1135-1145, 1979.

[3] Holt, B.J., Drift Scintillation Meter, AFGL-TR-84-0103, Air Force Geophysics Laboratory, Hanscom AFB, MA, March 1984. ADA142523.

[4] Smiddy, M., Sagalyn, R.C., Sullivan, W.P., Wildman, P.J.L., Anderson, P., and Rich, F., The Topside Ionosphere Plasma Monitor (SSIE) for the Block 5D/Flight 2 DMSP Satellite, AFGL-TR-78-0071, Air Force Geophysics Laboratory, Hanscom AFB, MA, March 1978. ADA058503.

[5] Rino, C.L. and Fremouw, E.J., "The Angle Dependence of Singly Scattered Wavefields," J. Atmosph. Terr. Phys., 39, pp 859-868, 1977.

[6] Fougere, P.F., "On the Accuracy of Spectrum Analysis of Red Noise Processes Using Maximum Entropy and Periodogram Methods: Simulation Studies and Application to Geophysical Data," J. Geophys. Res., 90, 4355-4366, 1985.

[7] Secan, J.A. and Bussey, R.M., DMSP SSIES Flight Data Processor System Documentation, PD-NW-85-336R, Volumes II and IV, NorthWest Research Associates, Inc., Bellevue, WA, 1986.

[8] Secan, J.A. Development of Techniques for the Use of DMSP SSIE Data in the AWS 4D Ionosphere Model, AFGL-TR-85-0107(I), Air Force Geophysics Laboratory, Hanscom AFB, MA, April 1985. ADA176412.

[9] Bilitza, D., "The Atmospheric Explorer C Ionospheric Temperatures: Dependences and Representation," Report UAG-90, World Data Center for Solar-Terrestrial Physics, Boulder, CO, pp. 114-122, May 1984.

[10] LLewellyn, S.K. and Bent, R., Documentation and Description of BENT Ionospheric Model, AFCRL-TR-73-0657, Air Force Geophysics Laboratory, Hanscom AFB, MA, 1973. AD772733.

[11] Damon, T.D. and Hartranft, F.R., Ionospheric Electron Density Profile Model, Technical Memorandum 70-3, Aerospace Environmental Support Center, Ent AFB, CO, July 1970 (available from the USAF Air Weather Service Technical Library, Scott AFB, IL 62225).

[12] Flattery, T.W. and Ramsay, A.C. "Derivation of Total Electron Content for Real Time Applications," Effect of the Ionosphere on Space Systems and Communications, Naval Research Laboratory, Washington, DC, pp. 336-344, 1975.

Appendix A. Data Sets Used in Studies

A.1 Simulated Data Sets

In order to measure the effectiveness and accuracy of the various techniques used in calculating C_k from a plasma density data sample, two sets of simulated density data with known spectral characteristics were generated. Such a data set can be constructed simply from

$$\Delta N_n = \sum_{i=1}^{N/2} a_i \sin\left[(i-\Delta i)\frac{2\pi n}{N} + \epsilon_i\right] \quad [A-1]$$

where ΔN_n is the nth density data point in the sample, N is the total number of points per data sample, Δi is a frequency shift parameter, ϵ_i is a random phase shift parameter (range: $-\pi$ to $+\pi$), and a_i is the amplitude. The frequency shift parameter, Δi, subtracted from i in calculating the argument of the sine function, is used to shift the power in the data set to frequencies away from frequencies of the discrete FFT used to calculate estimates of the spectral density functions from the data sets. This is done to maximize the effects of spectral "leakage" between spectral frequency bins. For example if $\Delta i = 0$, all power is located at the FFT frequencies and no leakage will occur. If, on the other hand, $\Delta i = 1/2$, all power is located at frequencies halfway between the FFT frequencies, which will provide a measure of the maximum spectral leakage.

The amplitude, a_i, is given by

$$a_i = 2\sqrt{\Phi_i \, \Delta f} \quad [A-2]$$

where Δf is the frequency step (24/N for SSIES data sets), and Φ_i is the desired power density spectrum (PDS) for the sample. For our studies, we assume that the PDS can be described by a power law of the form

$$\Phi_i = T_1 f_i^{-q} \quad [A-3]$$

where T_1 is the PDS value at a frequency of 1 Hz and q is the slope of the PDS. The frequencies to use in Equation [A-3] are given by $f_i = (i-\Delta i)\Delta f$, so combining Equations [A-2] and [A-3], the amplitude then becomes

$$a_i = 2\sqrt{T_1 \; \Delta f^{-(q-1)} \; (i-\Delta i)^{-q}}. \qquad [A-4]$$

As we may want to set up different samples for different levels of irregularity strength (T_1), we define a normalized density sample by

$$\langle \Delta N_n \rangle = \frac{\Delta N_n}{T_1} \quad . \qquad [A-5]$$

Using Equations [A-1], [A-4], and [A-5], the normalized density is calculated from

$$\langle \Delta N_n \rangle = 2\Delta f^{-(q-1)/2} \sum_{i=1}^{N/2} (i-\Delta i)^{-q/2} \sin\left[(i-\Delta i)\frac{2\pi n}{N} + \epsilon_i\right]. \qquad [A-6]$$

We can also define a normalized $RMS\Delta N_n$, $\langle RMS \rangle$, from

$$\langle RMS \rangle = \left(\frac{\sum \Delta N_n{}^2}{N}\right)^{1/2} = T_1{}^{1/2} \; RMS\Delta N_n \; . \qquad [A-7]$$

Therefore, given q, we can specify a normalized density sample and RMS; and given T_1, we can calculate the desired density sample and the $RMS\Delta N_n$ for the sample from

$$\Delta N_n = T_1{}^{1/2} \; \langle \Delta N_n \rangle \qquad [A-8]$$

and

$$RMS\Delta N = T_1^{1/2} \langle RMS \rangle \quad . \qquad [A-9]$$

In the studies presented here, two sample data bases were constructed containing six 2048-point realizations for each q value in the set $q:q = 1.0, 1.2, 1.4, \ldots, 2.8, 3.0$, one data base for the zero-leakage case, $(\Delta i = 1/2)$. Figure A-1 shows one of the realizations from each data base for $q = 1.6$, and Figure A-2 shows the PDS constructed from each realization (note that the PDS for the zero-leakage case is shifted up a decade on the plot). No windowing or detrending was done in constructing these PDS estimates, and the effects of the spectral leakage from the maximum-leakage case are quite evident. The variation of RMS as a function of q for the two simulation data bases is shown in Figure A-3.

In order to study detrender effects, it was decided to add more terms to Equation [A-6] with wavelengths longer than the data sample size. The frequencies for these additional terms were selected as $0.25\Delta f$, $0.5\Delta f$, and $0.75\Delta f$. All three are added to the zero-leakage cases, but only the $0.25\Delta f$ and $0.75\Delta f$ terms are added to the maximum-leakage cases, as the $0.5\Delta f$ term has already been included in Equation [A-6]. These terms were added on as density trends during the parametric studies rather than directly to the simulation data bases. This was done so that the zero-leakage data samples could be used as "sanity checks" for the processing software, since they should return a straight-line PDS when the data are neither detrended nor windowed, as in Figure A-2.

A.2 WIDEBAND Phase Scintillation Data Set

No *in situ* plasma density data sets were available for this study. Fortunately, a large body of phase scintillation data is available at NWRA from both the WIDEBAND and HiLat beacon experiments. While these data are not direct measures of the one-dimensional *in situ* density spectrum, they do provide a measure of the two-dimensional spectrum and have similar characteristics, i.e., they can be approximated by a red-noise power-law spectrum.

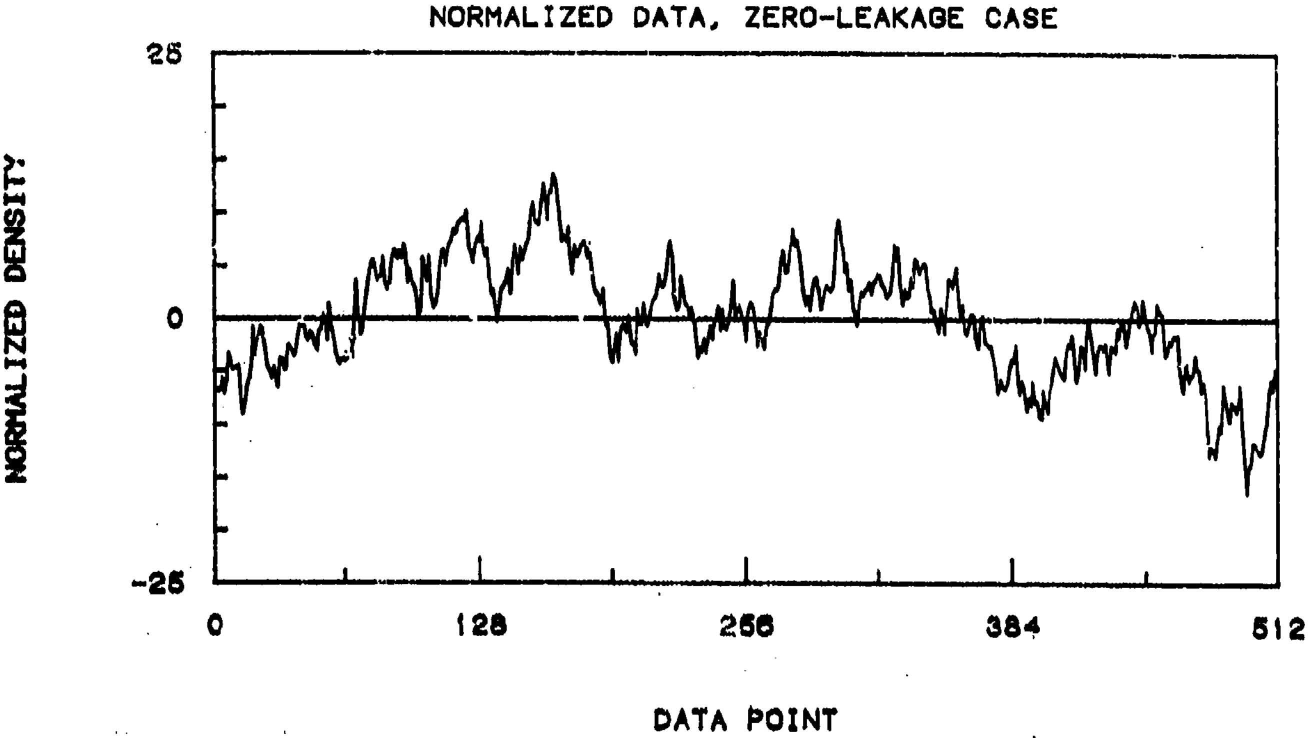

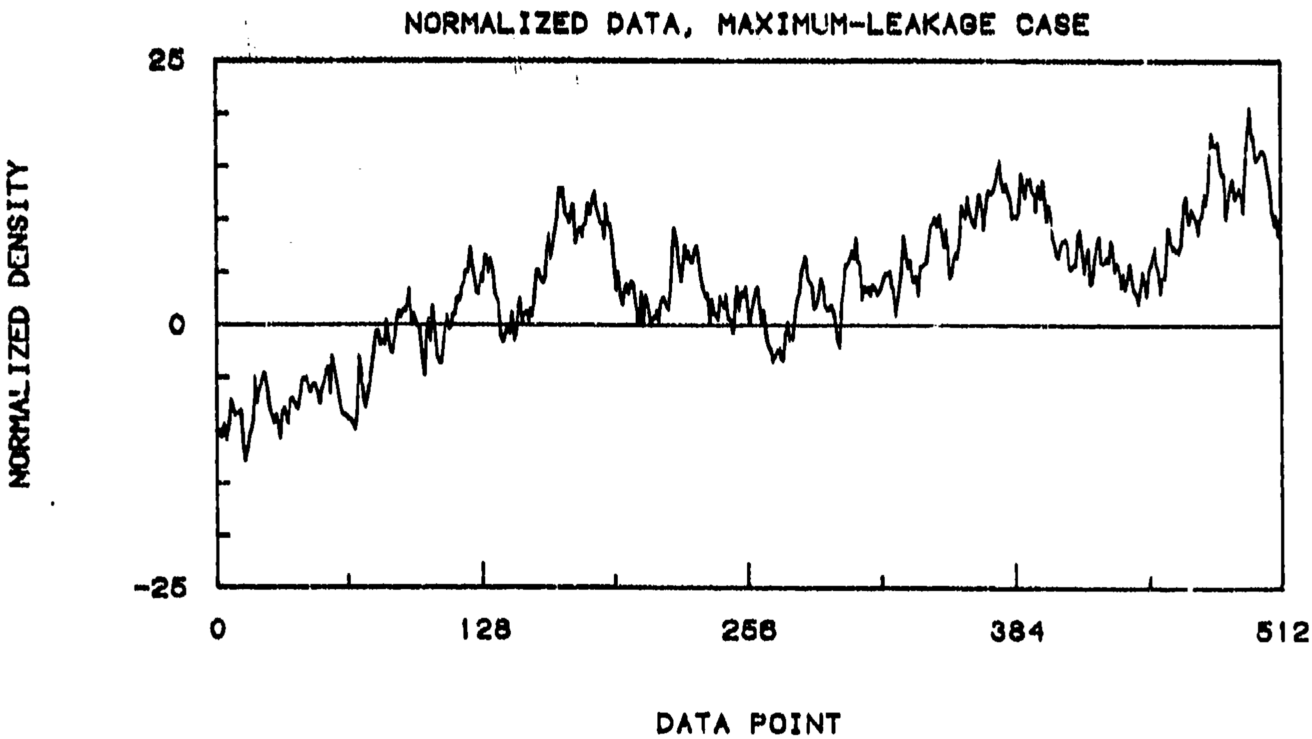

Figure A-1. Data samples from the zero-leakage (upper plot) and maximum-leakage (lower plot) for q = 1.6

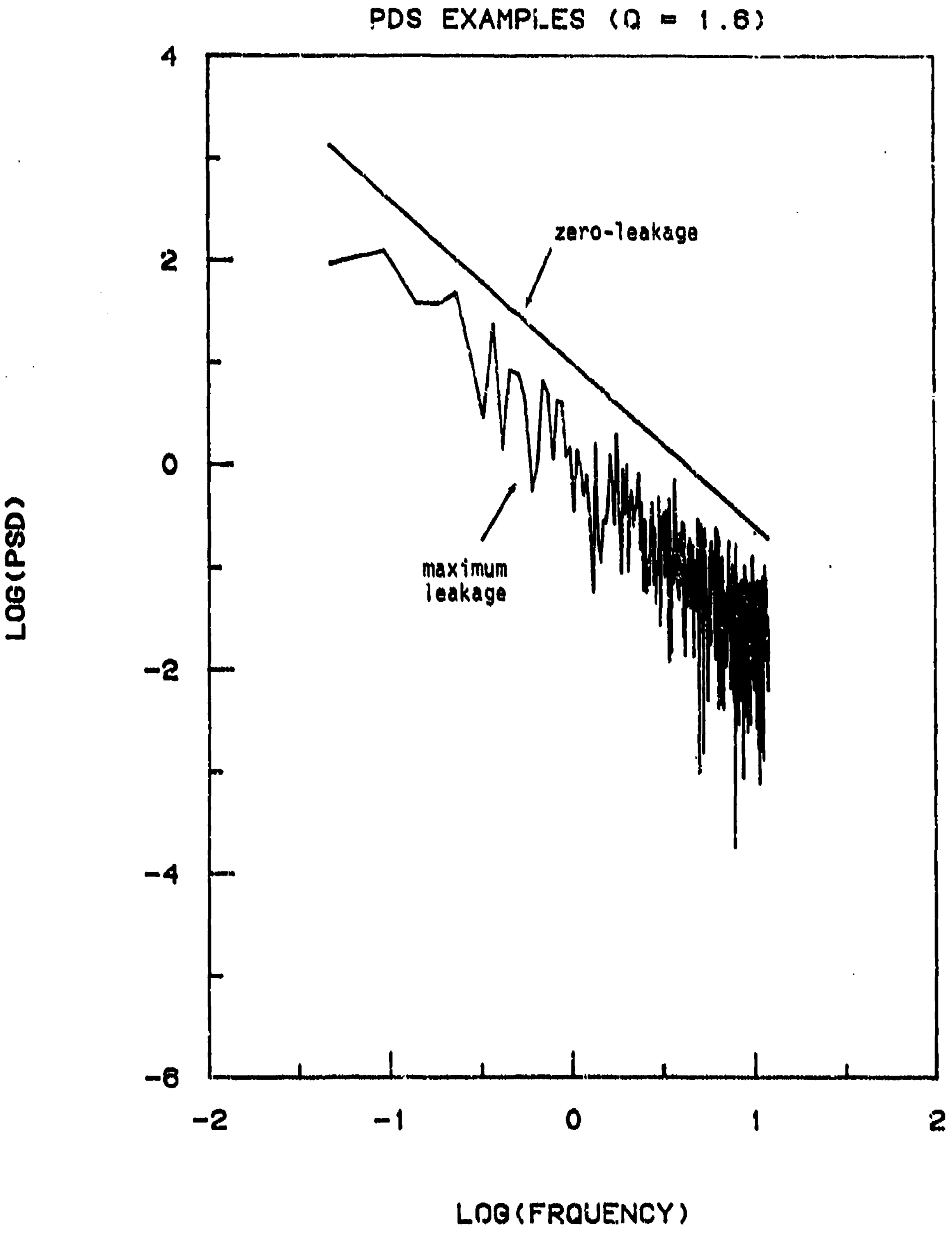

Figure A-2. Power density spectra of the data in Figure A-1.

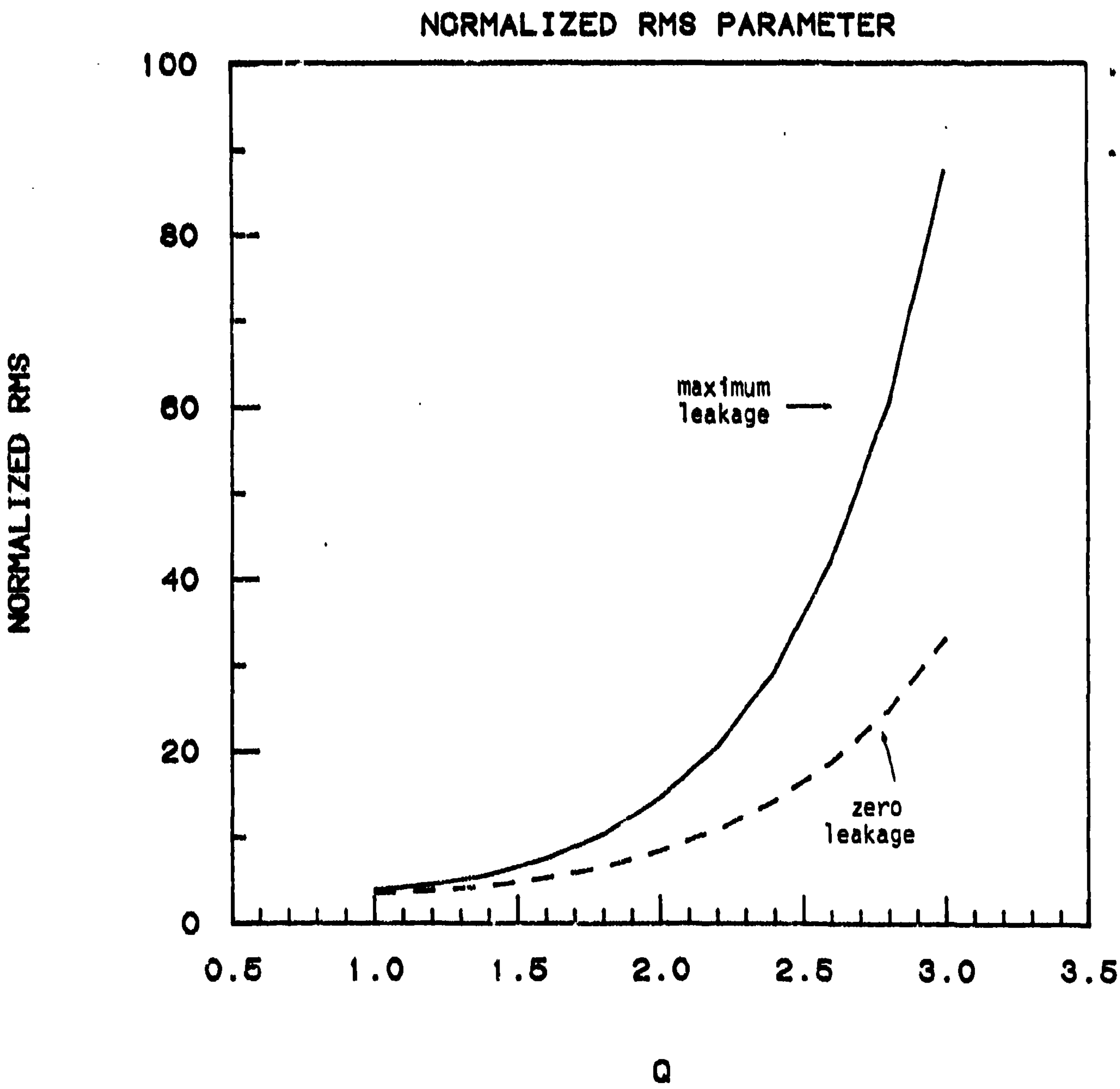

Figure A-3. Variation of RMS with q for the zero- and maximum-leakage data sets.

A single WIDEBAND satellite pass at the Poker Flat, Alaska, receiving site was selected for this study (pass PF-52-47). Figure A-4 shows plots of the phase data from this pass. The upper plot in this figure is the raw phase record for the pass. The lower plot is a detrended phase obtained by removing a low-pass trend calculated using a 6-pole Butterworth filter similar to one used in routine WIDEBAND processing. In this case, the 6dB cutoff frequency was set at 0.03333Hz (a 30 second detrend time). For this study, the phase data are reduced from the full sampling rate of 500Hz down to 25Hz. A total of 64 data samples are extracted from the pass by selecting 512-point data samples at 256-point intervals throughout the pass.

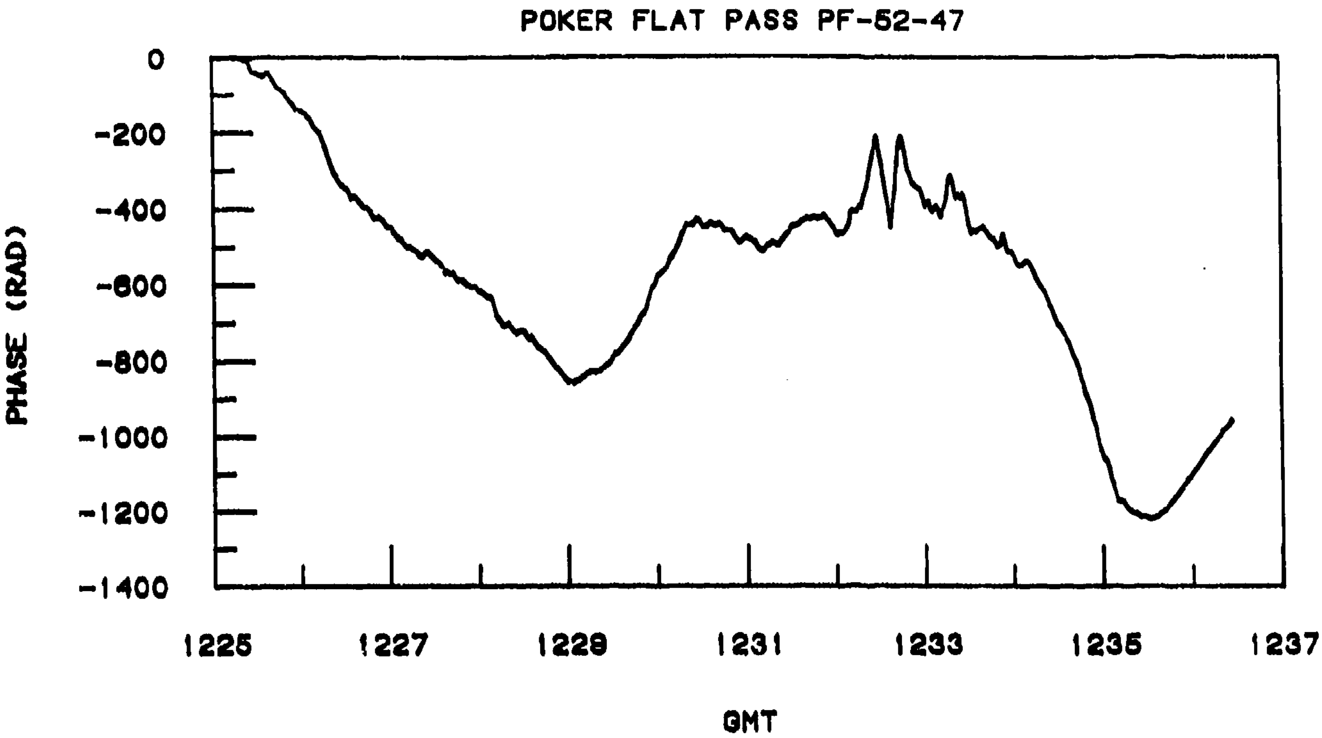

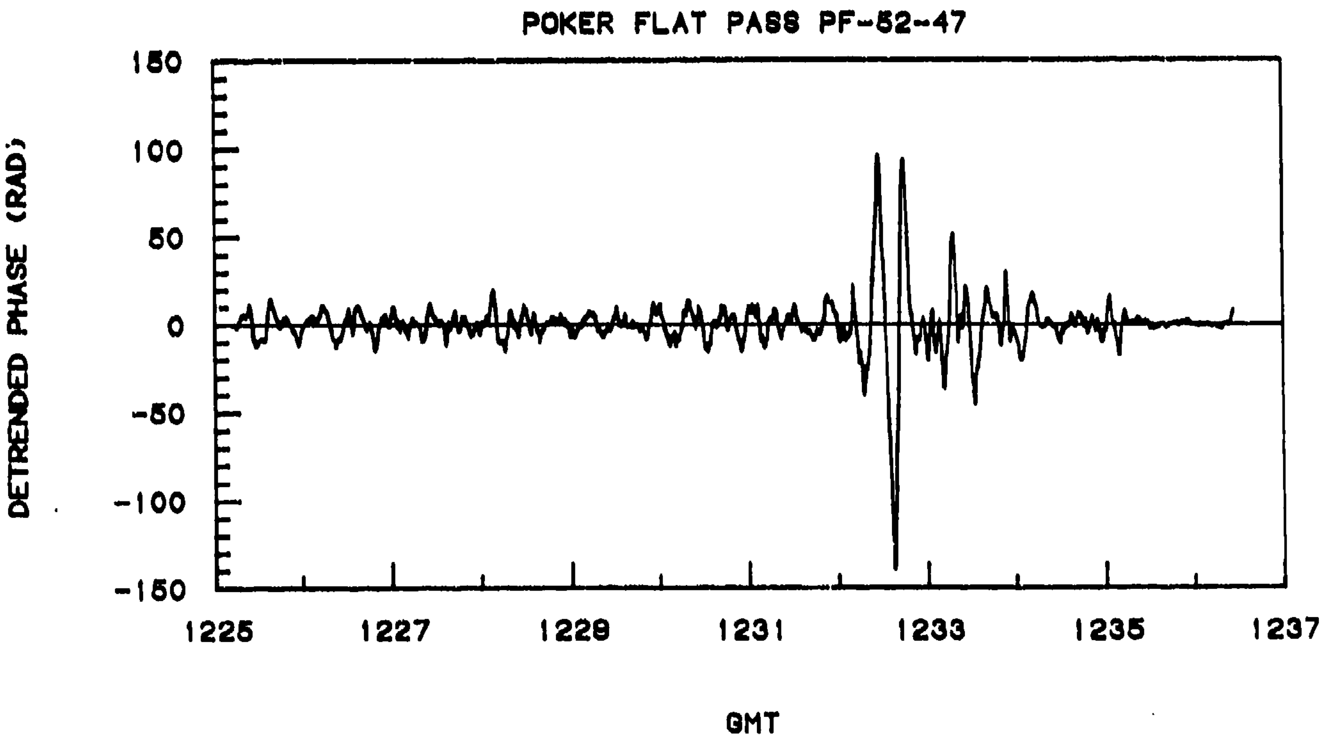

Figure A-4. Phase scintillation from WIDEBAND/Poker Flat pass PF-52-47. Upper plot is the raw phase record; lower plot is the detrended phase obtained by removing a low-pass filter trend.

Appendix B. Topside Electron Density Model

The electron density profile model used in this study was developed specifically for use with the DMSP SSIES sensor package.[8] The underlying structure of the topside section of the model is that of a two-component ionosphere (O+ and H+) in diffusive equilibrium, but it has been parameterized to allow the model to be fit to non-equilibrium conditions. Assuming charge neutrality, the electron density profile will be identical to the height variation of the ionospheric plasma density, which for this model is given by

$$N_e(h) = N_p(h) = \left(\frac{T_{po}}{T_p}\right) e^{\beta\mu} \left[N_o(O+)e^{-16\alpha I} + N_o(H+)e^{-I}\right] \qquad [B-1]$$

$$\alpha = \alpha_0 + \alpha_1(h-400) \qquad [B-2]$$

where T_p is the plasma temperature (T_i+T_e); T_{po} is the plasma temperature at a reference height (h_o); $N_o(O+)$ and $N_o(H+)$ are the number densities of O+ and H+ at the reference height; α_0, α_1, and β are profile adjustment parameters; and μ and I are integral functions given by

$$\mu(h) = \int_{h_o}^{h} \left(\frac{T_e}{T_i}\right)\left(\frac{m_+ g}{kT_p}\right)\left(\frac{16+R}{1+R}\right) dh \qquad [B-3]$$

$$I(h) = \int_{h_o}^{h} \left(\frac{m_+ g}{kT_i}\right) dh \qquad [B-4]$$

where m_+ is the mass of H+, and R is defined as the ratio of N(O+) to N(H+). Ion and electron temperatures are obtained from a recent model based on an analysis of data from the AE-C satellite.[9] The density ratio, R, is based on the O+ to H+ transition height, h_T, defined as the height at which N(O+) = N(H+). This parameter can be either (1) calculated from observations of N(O+), N(H+), and T_p from the SSIES

RPA sensor, or (2) obtained from an empirical model of h_T derived from published analyses of topside profiles from the Alouette satellites and RPA data from OGO-6.[8]

The topside model is fit to the F2 peak by means of a parabolic layer taken from the Bent profile model[10] of the form

$$N_e(h) = N_mF2 \left[1 - \left(\frac{h - h_mF2}{Y_t} \right)^2 \right] \qquad [B-5]$$

where N_mF2 and h_mF2 are the density and height of the F2 layer peak and Y_t is the parabolic semi-thickness. The Y_t parameter can be either estimated in the procedure used to fit the profile to observations, or obtained from the expressions used in the original Bent model. Equations [B-1] and [B-5] are fit together at the height where the plasma scale height calculated from the two representations of $N_p(h)$ are equal. This must be calculated iteratively, but rarely requires more that four or five iterations. This height is also used as the reference height, h_o, for the parameters in Equation [B-1].

For the sake of providing a complete plasma density profile, the bottomside section of the Air Weather Service (AWS) RBTEC model is used to describe the height variation below the F2 peak.[11,12] This model uses three Chapman-function layers to describe the three main ionospheric layers (E, F1, and F2). The choice of models for the bottomside of the profile has little impact on the present study, as the irregularity layer is assumed start either at or just slightly below the F2 peak.

A number of techniques were devised for fitting this profile model to a wide range of input data. For the application at hand, we will assume that an observation of N_p at the satellite altitude is available, and that an observation of f_oF2 and h_mF2 may or may not be available. If all three are available, the profile can be adjusted to fit all three by adjusting any two of the four parameters, Y_t, β, α_o, or α_1. If either f_oF2 or h_mF2 is missing, a profile can be fit to the density at the satellite and the available F2-layer parameter providing an estimate of the missing F2-layer parameter assuming fixed values for Y_t and the three adjustment parameters.